Development of the analyser module for the MIDAS Data Acquisition System operating on the K600 magnetic spectrometer at iThemba LABS, Cape Town

Stephen David Jones

February 2008

Thesis submitted in fulfilment of
the requirements for the degree of Master of Science
at the University of Cape Town

Abstract

The focal-plane detector package at iThemba LABS, Cape Town, is reviewed and a new analyser module is developed. The mathematical methods employed by the analyser are also reviewed and the final system is calibrated and tested against experimental data taken at iThemba LABS, Cape Town.

Declaration

1. I know that plagiarism is wrong. Plagiarism is to use another's work and to pretend that it is one's own.
2. I have used an accepted convention for citation and referencing. In this thesis, each significant contribution or quotation from the work or works of other people has been attributed, and cited or referenced.
3. This thesis is my own work.
4. I have not allowed, and will not allow, anyone to copy my work with the intention of passing it off as his or her own work.

....

Stephen David Jones

Contents

List of Figures

Chapter 1

Introduction

iThemba LABS (Laboratory for Accelerator Based Sciences), Cape Town, formerly the National Accelerator Centre (NAC), is both the foremost accelerator centre in South Africa and a medical radiation treatment facility, which focuses on the treatment of inoperable tumours using proton and neutron therapy. Administered by the National Research Foundation (NRF), iThemba LABS, Cape Town, is home to a number of physics research groups, focusing on applied and pure sub-atomic sciences, as well as four primary sub-atomic particle accelerators [24].

The largest of these accelerators is the K200 Separated Sector Cyclotron (SSC), which is able to accelerate protons to energies up to 200 MeV (typically used in proton therapy), as well as light and heavy ions to greater energies. There are also two injector cyclotrons, which produce either an intense beam of unpolarised light ions, a less intense beam of polarised light ions, or a beam of heavy ions for subsequent injection into the SSC. A 6MV Van de Graaf electrostatic accelerator is also on site [24].

One of the research groups, which relies critically on the accelerator facilities available at iThemba LABS, Cape Town, is that of fundamental nuclear and particle physics. This research focuses on experimental studies of the properties of nuclei at moderate to high excitation energies and angular momenta, as well as the various mechanisms and interactions through which these reactions occur. The primary experimental set-ups currently in use are the AFRODITE (AFRican Omnipurpose Detector for Innovative Techniques and Experiments) gamma-ray array and the K600 magnetic spectrometer. Gamma-ray spectroscopy is performed with AFRODITE, while light charged particles emitted in nuclear reactions are studied with the K600 magnetic spectrometer. The particle beam used to power these experiments is accelerated by the SSC.

1.1 The K600 Magnetic Spectrometer

1.1.1 Basic Structure

The K600 magnetic spectrometer[1] is based on the K600 spectrometer at Indiana University's Cyclotron Facility. It consists of five primary elements, namely a quadropole magnet, two dipole magnets and two trim coils (termed K and H coils). A schematic diagram of the K600 magnetic spectrometer is shown in Figure 1.1 below.

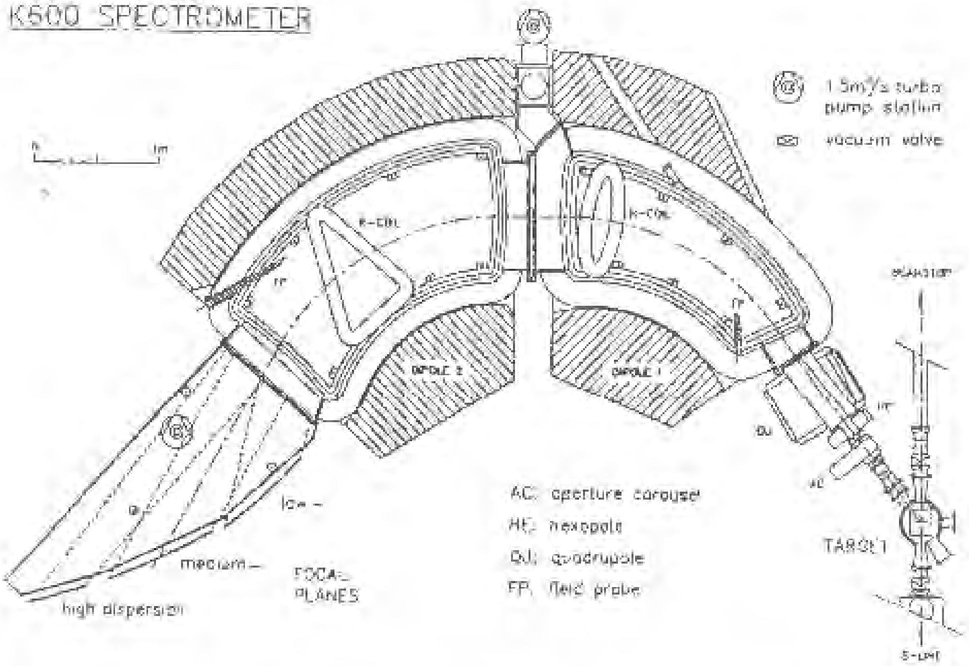

Figure 1.1: A schematic view of the K600 magnetic spectrometer [19].

At the turning axis of the spectrometer is a scattering chamber with a 524mm diameter, which contains a target ladder with six target positions. In addition, there is also a turntable inside the scattering chamber on which detec-

---

[1] Also known as the K600 light ion spectrometer

tors can be mounted [19]. Downstream, along the chosen scattering path, is a carousel containing six collimators, and then the quadrupole magnet and the rest of the K600 magnetic spectrometer.

To get a rough indication of the size of the spectrometer, the average path length for an incident particle, from the scattering chamber to the detector, is approximately 8m. The K600 magnetic spectrometer offers good energy and momentum resolution when measuring light charged particles such as protons to alpha particles.

1.1.2 Trajectory Reconstruction from Target Chamber to Focal-Plane

Once the proton beam has been accelerated by the SSC, it enters the 524mm scattering chamber via the S-line beam pipe displayed in Figure 1.1. It then impinges upon the experimental target, which is situated on the target ladder inside the scattering chamber. On exiting this target chamber, the scattered protons are collimated by one of the collimators, which are mounted on the aperture carousel and define the angular position and the size of the solid angle of protons entering the K600 magnetic spectrometer.

To facilitate measurement at both small and large angles, the K600 magnetic spectrometer makes use of two beam stops: An internal Faraday cup, for small angle measurements, and a larger, external beam stop for measurements at large angles [12].

Once the scattered protons have been collimated, they enter the ion-optical system of the K600. This ion-optical system consists of five active elements (previously mentioned): One quadrupole magnet, two dipole magnets and two trim coils. The quadrupole magnet is used for vertical focusing, while the two dipole magnets are used to bend the proton beam in the horizontal plane [19, 12]. Each dipole magnet has its own focusing coil. The first dipole magnet makes use of the H correction coil as a hexapole focusing element to correct for second-order aberrations, while the second dipole magnet makes use of the K correction coil as a quadrupole focusing element to correct for first-order variations of momentum with angle [19, 12].

The result of the ion-optical system is that the incoming scattered protons are focused on the focal-plane, where a position-sensitive detector package is mounted. This detector package has been recently upgraded from a set of two vertical drift chambers and one horizontal drift chamber to a new system consisting of two drift chambers, each containing a vertical wire-plane and a slanted wire-plane. These detectors measure particle information in the focal-plane as well as in the plane perpendicular to the focal-plane [19, 12, 13].

Two plastic scintillator detectors are located downstream from the drift chambers. These paddle detectors act as low level triggers as well as particle identification detectors [19].

1.2 Objectives and Outline of Thesis

1.2.1 Objectives

The upgraded detector package mentioned above offers a higher resolution than its predecessor, particularly in the plane perpendicular to the focal-plane. This increase in resolution is a result of an increased number of channels per detector, which has prompted the upgrade of the data acquisition electronics from a CAMAC based system to a VME system. This, in turn, necessitated the redesign of the data acquisition software.

The work presented in this thesis focuses on a review of the design and operational characteristics of the new focal-plane detector package, as well as the design; implementation and testing of the analyser component to the new data acquisition software system.

1.2.2 Chapter Outlines

Chapter 2 begins by introducing the precursors to the experimental hardware used at iThemba LABS, namely the proportional counter and the multi-wire proportional counter. As the choice of fill gas plays an important role in both the experimental characteristics and potential detector diagnostics of the multi-wire proportional counter, various popular choices of fill gas are discussed and their effects on the detector explained. These ideas are then extended to the drift chamber and, more specifically, to the drift chambers in operation at iThemba LABS, both for the old and the newly-upgraded focal-plane detector packages. Chapter 2 concludes with a detailed description of the remaining components of the detector package, namely the time-to-digital converters used to measure timing information and the plastic scintillator detectors, which generate triggering information and are involved in particle identification.

The next chapter, Chapter 3, reviews the mathematical methods used in trajectory reconstruction in both the X and U-planes. A linear least squares regression method of straight line-fitting is implemented, but is found to yield inaccurate results. The reason for this inaccuracy is determined and a second, more robust, line-fitting technique is implemented.

Chapter 4 involves the application of these mathematical methods in the development of an algorithm for trajectory reconstruction, in both the X and U-planes, for use in the new detector package. Included in these algorithms is the geometric argument used to calculate vertical position using the slanted wire-plane, as well as horizontal position using the vertical wire-plane. Chapter 4 concludes with a calculation of the expected resolution of the new detectors in both the X and U-planes.

The customised analyser module is introduced in Chapter 5, together with the software framework in which it is designed to function (MIDAS). The program flow of the customised analyser is outlined and a detailed, step-by-step explanation of each stage is presented. These stages include: integrating the new analyser module into the existing MIDAS framework, reading and manipulating data from the online database, locating the necessary event information, correcting the raw experimental time data for differences in system and timing processor speeds as well as cabling effects, sorting the event data information into logical data structures representative of the physical detector, checking the corrected raw data to ensure that valid events were observed, and the implementation of the line-fitting techniques and trajectory reconstruction algorithms mentioned in Chapters 3 and 4.

The penultimate chapter, Chapter 6, deals with the testing of the developed analyser module using data taken from an experiment in which a proton beam was incident on a ^{12}C target. A discussion of possible future developments and some concluding remarks are presented in Chapter 7.

Chapter 2

Review of the Experimental Hardware at iThemba LABS

The experimental setup at iThemba LABS, Cape Town, comprises the K600 Magnetic Spectrometer and a newly updated focal-plane detector package. The focal-plane detector package consists of two Multi-Wire Proportional Counters (MWPCs), each containing two wire-planes. The vertical wire-plane is used to measure position and angle information in the focal-plane, whereas the slanted wire-plane is used to measure position and angle information perpendicular to the focal-plane [19]. Chapter two seeks to catalog and review both the theoretical design and practical construction of the multi-wire proportional counters used at iThemba LABS.

2.1 The Proportional Counter

Before one can begin to understand the Vertical Drift Chambers (VDCs) used at iThemba LABS, one must first understand the underlying principles of the proportional counter and the Geiger-Müller tube as these were some of the first electrical devices developed for use in modern radiation detection [22]. Although the Geiger-Müller tube and the proportional counter differ only slightly in their construction [22], the conditions under which they operate do indeed differ. These differing conditions (primarily the potential at which the wires are kept and the gas used to pressurize the chambers) allow us to exploit various ionization phenomena and give rise to many practical applications of proportional counters, which will be discussed later.

A simple proportional counter can be described as a cylindrical container with conducting walls and a thin window located at one end [1]. This cylinder is then filled with a gas, usually an inert gas such as argon. Along the central axis of the cylinder is suspended a conducting wire, which is kept at a constant positive voltage, say V_0, relative to the conducting walls of the cylinder. A simple proportional counter is depicted in Figure 2.1 below:

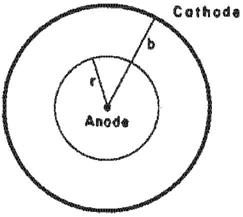

Figure 2.1: Front-on view of a simple proportional counter [1]

When a positive voltage V_0 is applied to the wire, a radial electric field, E, is produced inside the counter. This electric field has the form [1]:

$$E = \frac{1}{r}\frac{V_0}{\ln\left(\frac{b}{a}\right)}, \tag{2.1}$$

where r is the radial distance from the axis, b is the inside radius of the cylinder and a is the radius of the axial anode wire. This radial electric field is visualized in Figure 2.2.

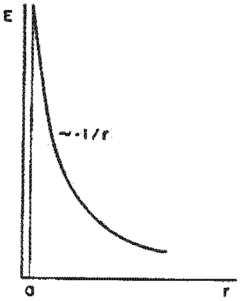

Figure 2.2: Visualisation of the radial electric field set up inside a proportional counter

Let us now examine what happens when radiation enters the cylinder. Upon entering, the radiation interacts with the pressurized gas, thus ionizing it in several places throughout its volume. This ionization results in electron-ion pairs, which are created directly in the case of charged particle radiation and indirectly, through secondary reactions, for neutral radiation [1].

Clearly the mean number of electron-ion pairs created is proportional to the energy deposited in the cylinder and thus proportional to the energy of the incident radiation. Once these electron-ion pairs are created they will immediately be accelerated in opposite directions by the radial electric field E. This acceleration causes the electrons to move towards the anode wire, while the positive ions are accelerated towards the cathode wall of the cylinder.

Once the electrons reach the anode wire they are collected and generate an electric current, which is interpreted as a signal. The magnitude of this current depends on the intensity of the electric field, E. This dependence is shown in Figure 2.3 below, which relates the number of ions collected to the anode wire voltage:

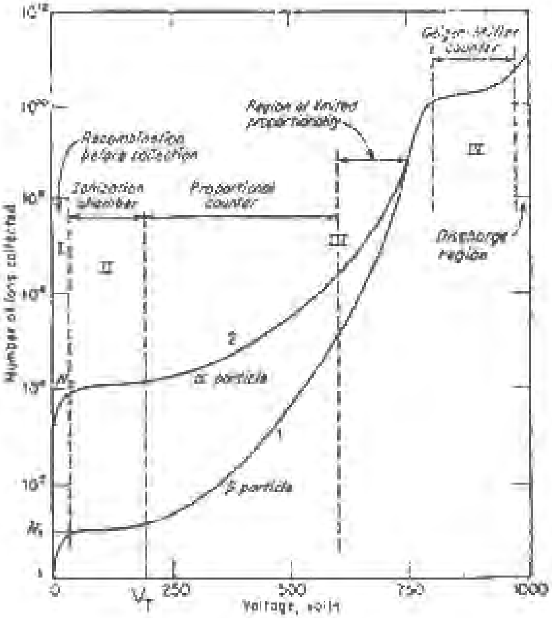

Figure 2.3: Figure illustrating the relationship between gain and voltage inside a proportional counter [1, 3].

As can be seen from Figure 2.3, when the wire voltage, V_0, is zero, no ions are collected as, in the absence of an electric field, the electron-ion pairs recombine under the action of the electric force between the liberated electron and its donor ion [1].

As the anode-wire voltage is increased, the number of ions collected increases as the force causing the electron-ion pairs to recombine is overcome by the electric field of the anode-wire. This region is the first flat region in figure 2.3, located in section II.

Detectors that operate at this voltage are termed ionization chambers as they work by collecting the ionized particles produced by direct reactions with the incident radiation [1].

If we continue to increase the anode-wire voltage past region II, we once again observe that the signal current increases with increasing voltage. The reason for this is that the electric field, E, is now strong enough to accelerate the liberated electrons to the point at which they have enough energy themselves to liberate additional electrons through inelastic collisions. These newly created electrons liberate further electrons and those in turn liberate even more. The resulting scenario is known as a Townsend avalanche [15]. From equation (2.1) we can infer that the electric field is strongest nearest the wire, which localizes the avalanche to within a few radii of the anode-wire.

The number of electrons that collect at the anode remains proportional to the number of electrons directly liberated by the incident radiation as the Townsend avalanche is a property of the applied voltage. There is hence an amplification of the signal current, with a multiplication factor dependent on V_0. This scenario is a desirable one as it produces a signal current far greater than the ionization chamber, yet is still proportional to the number of primary electrons. Detectors that operate at this voltage, located between regions II and III, are termed proportional counters.

If the anode-wire voltage is further increased beyond region III, the total number of ionized particles created is sufficiently large that their collective space charge distorts the electric field near the anode-wire. As can be seen from Figure 2.3, proportionality begins to be lost and this region is thus termed the region of limited proportionality [1], which is located between sections III and IV of the graph.

If the voltage is now increased beyond the region of limited proportionality, we reach the last useable voltage region, known as the Geiger region [4]. In this region the voltage is so high that excitations are observed in the atoms and molecules of the pressurized gas. These atoms and molecules then de-excite, by the emission of ultraviolet photons, causing a further chain reaction of ionisation avalanches [4] spread out over the entire length of the anode wire [1].

The result of this chain reaction is that the signal current becomes saturated – that is to say it always registers the same high amplitude for all incident radiation regardless of the energy of that radiation. The downfall of this signal current saturation is that detectors operating within this Geiger region do not give any information as to the type or energy of the incident radiation [4] – these parameters have to be inferred from the observation of shielding effects. Detectors operating within this region are termed Geiger-Müller or breakdown detectors and require an additional gas to act as what is known as a quenching gas [1]. The role of this quenching gas is to absorb the ultraviolet photons emitted by atomic or molecular de-excitation and drain their energy into other channels [1] to prevent current saturation.

If the voltage is increased further than region IV, a spontaneous breakdown occurs within the detector and a signal current is generated with or without the presence of ionising radiation. This is clearly undesirable and usually results in arcing and a damaged detector.

2.2 The Multi-wire Proportional Counter

Earning its inventor, Georges Charpak, the 1992 Nobel Prize in physics, the multi-wire proportional counter is the logical successor to the simple proportional counter discussed earlier [25]. Prior to the advent of the MWPC much particle detection in physics laboratories was facilitated by the use of bubble chambers. These well known devices were chambers filled with an overheated liquid which produced tracks of tiny boiling bubbles along the trajectory of the incident particles [17]. The downside of these detectors was that the particle tracks could only be viewed from optical photographs taken at one second intervals. Modern experiments typically produce hundreds to millions of events per second [17], which far exceeds the limitations imposed by bubble chambers. In addition, bubble chambers offered no projection information; instead the experimenter was restricted to a top-down view.

Charpak's discovery set in motion the development of a wide range of wire chambers, some of which are still in use today.

The basic MWPC can be considered as a plane of thin, parallel and equally spaced anode wires housed within two cathode planes and the gas mixture. These cathode planes can either be a mesh of conducting wires or a plane of conducting material, such as aluminised mylar [1]. The separation distance between the anode and cathode planes is typically of the order of a few millimetres [14]. The planes are then housed within a chamber and pressurised with a gas. As previously discussed, the choice of gas is important to the mode of operation of the detector and will be dealt with separately later. A simple MWPC is shown below:

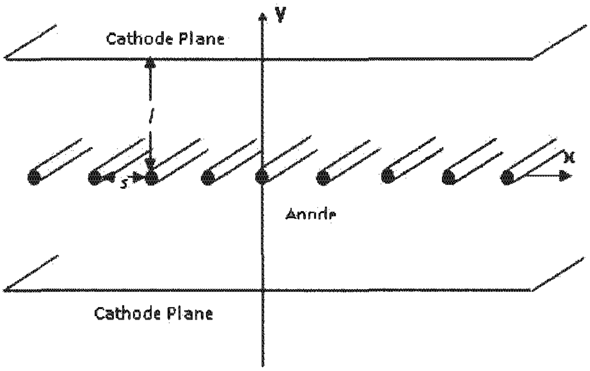

Figure 2.4: A side-on schematic view of a simple multi-wire proportional counter.

Figure 2.4 illustrates that a MWPC can be thought of as a side-by-side configuration of proportional counters with a mesh or plane acting as a cathode, rather than the walls of a conducting cylinder. When a high voltage (HV) is applied between the anode and cathode planes, an electric field is set up as in Figure 2.5

As can be seen from Figure 2.5, the electric field, E, is roughly constant for distances greater than fifteen anode wire radii [14], while it takes on a $1/r$ dependence within a few (typically of the order of five) anode wire radii [15]. This electric field configuration is useful as it is only when the primary electrons, produced by ionising radiation, are near the anode-wires that they gain enough kinetic energy to create a Townsend avalanche described previously. This scenario ensures, at least in theory, that any given Townsend avalanche is localised to one anode wire rather than spilling over onto another. If one considers the MWPC to be used for position detection, it is immediately obvious that, should an avalanche spread across multiple anode wires, the position information gathered in the experiment would be flawed as it is meaningless for a particle to be in two places inside the detector at a

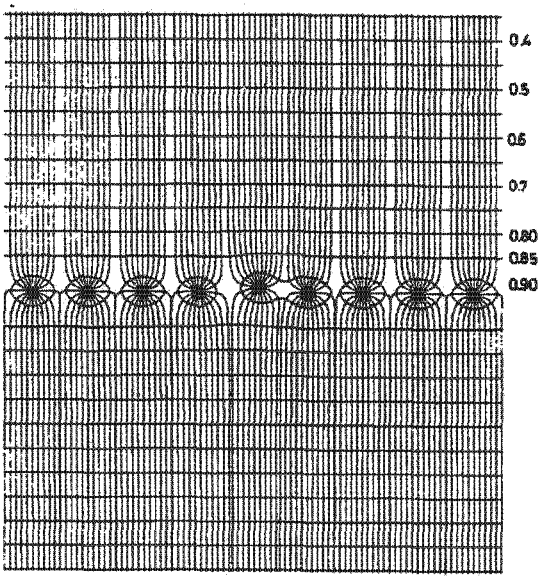

Figure 2.5: Electric field within a MWPC [1].

single point in time.

In real detectors, however, this constancy of electric field far away from the anode-wire plane is not enough to isolate the various anode wires and thus so-called guard wires are placed, evenly apart, between each anode wire in the plane [19]. These guard wires are beyond the scope of this idealised detector and will be treated in more detail later.

After the Townsend avalanche occurs, the current generated in each individual wire in the anode plane is amplified by electronics and interpreted as a separate signal. This signal current is then analysed further and physical quantities such as position and momentum may be calculated.

If the total charge collected within the detector is proportional to the total number of primary electrons, the detector is said to be operating within the region of proportionality or is termed a proportional detector. The constant of proportionality is called the multiplication factor and has a square dependence on the voltage applied to the anode-wire plane [14],

$$m \sim V_0^2. \tag{2.2}$$

Figure 2.6, taken from the journal of physics: conference series, illustrates the dependence of the multiplication factor, m, on the applied voltage.

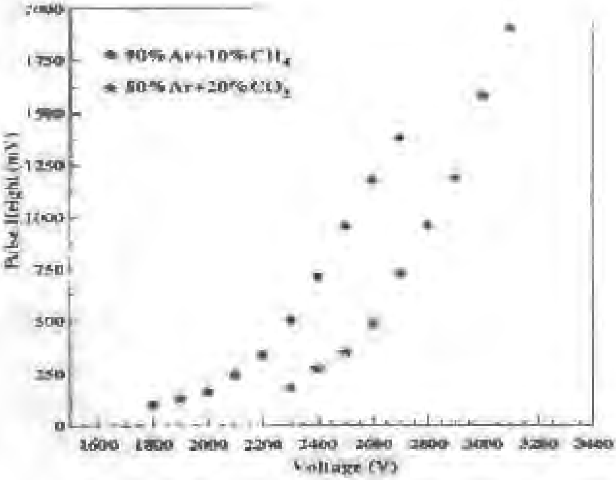

Figure 2.6: The dependence of the multiplication factor, m, on the applied high voltage [14].

2.2.1 Choice of Fill Gas

The operational characteristics of a MWPC depend greatly on the choice of fill gas. This choice is influenced largely by four factors [1]:

- Low working voltage: the fill gas must support avalanche production at as low a voltage as possible.
- High gain: the fill gas must give rise to sufficiently large avalanches to ensure that the final signal current is large when compared to background noise.
- Good proportionality: the total charge deposited in the detector must be proportional to the number of primary electrons.
- High hit rate capability: the fill gas must not change its operating characteristics when subjected to a high particle rate.

To meet the low working voltage requirement, inert gases are usually chosen as they yield avalanches for electric fields of low intensities [1] as illustrated in Figure 2.7. The preferred inert gas is argon as it is both inexpensive and has a high specific ionisation – that is to say when radiation passes through argon, a large number of electron ion pairs are created along the trajectory of the incident radiation [26].

Pure argon, however, only provides a gain of the order of 10^3 - 10^4 before the onset of continuous discharge, whereas a gain of 10^6 or greater is more desirable for modern physics experiments [1]. The reason for this discharge is the high excitation energy of argon (11.6 eV). When excited argon atoms de-excite they release 11.6 eV photons which, in turn, cause further avalanches. As the number of these unwanted avalanches increases, proportionality is lost as the charge deposited in the detector is no longer due only to the avalanches set in motion by primary electrons, but also has an increasing component due to high energy photons being emitted by de-exciting argon atoms.

This problem can be corrected by the addition of a so-called quenching gas. A quenching gas acts like a sponge in that it absorbs radiated photons and dissipates their energy through dissociation reactions and elastic collisions, which are not harmful to data acquisition [1].

In dissociative reactions the molecules of the quenching gas split into separate smaller ions or molecules upon contact with the incident photons, while in elastic collisions the high energy photons are Thompson-scattered [30] and absorbed.

The most common quenching gases are polyatomic gases such as CH_4 or alcohol. However, inorganic gases such as CO_2 or BF_3 can also be used [1]. With the addition of a quenching gas more acceptable gains (to the order of 10^6) are achieved. A mixture of 90% Ar and 10% CH_4 is frequently used and has been named P10 gas [1, 23].

One of the problems with P10 gas, as well as with any organic quenching gas, is the accumulation of solid or liquid polymers on the anode and cathode after the absorption of high doses of radiation. The manner in which the organic gas quenches the unwanted excited photons is the root of the problem. As mentioned earlier, a quenching gas works by dissociative reactions which split the quenching gas into smaller molecules. When these molecules recombine, they form solid or liquid polymers which adhere to the anode and cathode and form a layer. Both the positive and negative ions arriving at the anode and cathode planes must first diffuse through the polymer layer before arriving at their destinations. As the positive ions drift far more slowly than the electrons (by a factor of 10^{-3}), a positive charge build-up occurs within the detector [1]. Over time this charge build-up is so great that it causes a spontaneous discharge within the detector, which persists even after the removal of radiation. Once this occurs, the polymers must be removed from the detector before it can be used again. This problem can be avoided by using an inorganic quenching gas such as CO_2, although they offer lower resolution.

To keep the inherent efficiency of organic quenchers, while avoiding anode and cathode polymerisation, a third gas is added to the mixture. This third gas, methylal or propylic alcohol, acts as a nonpolymerising agent.

One final problem worth noting: when dealing with a sealed gas detector, the quenching gas itself is consumed. The more quenching gas consumed, the less effect the remaining gas will have within the detector until there is no quenching gas remaining and proportionality is lost [1, 15]. This problem can be circumvented by having a continuous gas flow within the detector rather than having it sealed.

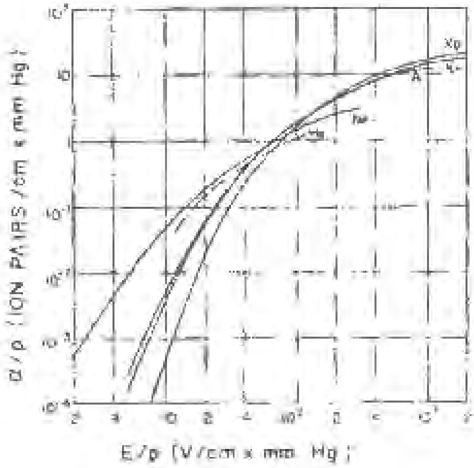

Figure 2.7: The probability of a secondary ionisation event per unit path length, also known as the first Townsend coefficient, is displayed as a function of reduced electric field for various inert gases [1, 15].

2.3 Drift Chambers

When the MWPC was first invented, it was envisioned as a speedy means of detecting radiation. During its infancy, however, it was realised that the

MWPC could also be used to determine spatial information, provided the drift time of ionised electrons was known [1]. If the arrival time of the incident radiation is known, as well as the time at which a given signal-wire fires, then the drift distance from the point at which the electron was ionised to the signal-wire can be written as [1]:

$$x = \int_{t_i}^{t_f} u(E)dt, \tag{2.3}$$

where t_i is the arrival time of the incident radiation, measured by electronic devices, t_f is the arrival time of the ionised electron at the anode-wire and $u(E)$ is the drift velocity of the ionised electron as a function of the applied electric field, E.

The generalised equation above requires an exact mathematical expression for the (possibly complicated) electric field. As it is impractical to expect a data acquisition system to dynamically integrate a computationally expensive function up to seven times per event, most drift chambers employ field shaping. These so-called field shaping wires are kept at a constant voltage, appropriate in magnitude and opposite in sign to the anode-wire voltage. The field shaping wires serve as a means to make the electric field close to the anode-wire constant as opposed to the $1/r$ dependence shown above in Figure 2.5 [1].

Employing this assumption reduces equation (2.3) above to:

$$x = u \int_{t_i}^{t_f} dt. \tag{2.4}$$

This yields a constant drift velocity, allowing the drift distance x to be precisely calculated. Once the drift distance or distances if multiple wires fire, are known, the trajectories of the incident particles can be reconstructed using methods which will be explained later.

2.3.1 Choice of Drift Chamber Fill Gas

As with the MWPC, the choice of drift gas in the chamber is vital. In addition to the factors described above, one must pay particular attention to the drift velocities of ionised electrons through the drift gases. Should the drift velocity be too small, or the drift path too long, then the presence of electronegative gases would absorb the ionised electrons before they reached the anode wire-plane, thus rendering the data useless.

It is ideal, therefore, to have the drift chamber gas as pure as experimentally possible. Using only a pure inert gas as a drift gas causes problems (explained earlier) and thus a small amount of impurity, in the way of quenching gases, etc, must be used. The extent of the impurity allowed is proportional to the length of the drift path. The longer the drift path of the ionised electrons, the more likely they are to be captured by the electronegative gases [1].

Another desirable quality for a drift chamber gas is the saturation of the drift velocity at low, or low enough, electric field intensities. This means that, for a small change in the homogeneity of the electric field, the drift velocity of electrons through the drift gas changes little [1]. Should the drift velocity change by a non-negligible amount, then formula (2.4) above would not be valid. The addition of guard wires would not alleviate the need for the time consuming integration that would be required for accurate data analysis.

Figures 2.8 and 2.9 below show the drift velocity of electrons in two gas chambers: one chamber containing various mixtures of argon and methane and the other chamber containing various mixtures of argon and ethylene [1, 2].

From the above figure we can observe that, for certain magnitudes of the electric field, the gas mixtures yield a roughly constant drift velocity for a large change in electric field. Other factors that influence the magnitude of the electric field are the chamber temperature, room temperature, operating voltage, quality of the electronics and wiring etc. Detectors whose drift gases operate in this region are thus less susceptible to the factors mentioned above.

Finally, the magnitude of the drift velocity itself also plays an important role in the mode of operation of the drift chamber. Should we want the chamber to be optimised for acquiring data at a rapid rate, then the drift velocity should be as large as possible to minimise dead time within the detector [1]. If, on the other hand, we wish our detector to acquire data more slowly, but give more accurate spatial data, then the drift velocity should be as small as possible so as to minimise the error in the timing measurements [1].

Gases which offer high drift velocities include: CF_4 mixed with a hydrocarbon quencher [1], while gases which yield lower drift velocities include: CO_2 or He mixed with C_2H_6 [1].

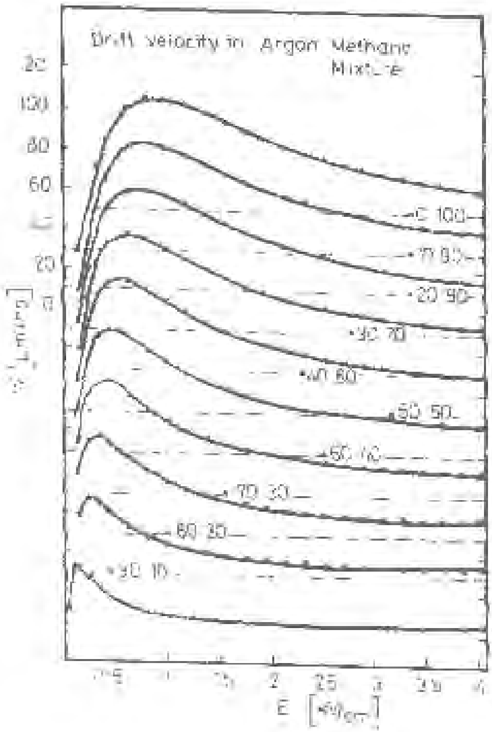

Figure 2.8: Drift velocity of electrons in an argon methane gas mixture, as a function of electric field [1, 2].

2.4 The Drift Chambers at iThemba LABS

There are two identical MWPCs in the K600 spectrometer vault at iThemba LABS. Each MWPC houses two anode-wire planes: one vertical wire plane, or X-plane, to facilitate the measurement of both the position and angle in the focal plane; and one slanted wire plane, or U-plane, to facilitate the measurement of the position and angle perpendicular to the focal plane [19]. The vertical and the slanted wire-planes will be treated separately, even though they are housed within the same detector, since the U-plane was added on to an already existing MWPC and, therefore, its construction depends on that original MWPC.

The original focal plane detector package contained three MWPCs: two vertical drift chambers, or VDCs, and one horizontal drift chamber, or HDC, which is shown in Figure 2.10. The words vertical and horizontal refer not to the orientations of the wire planes within the detectors but rather to the

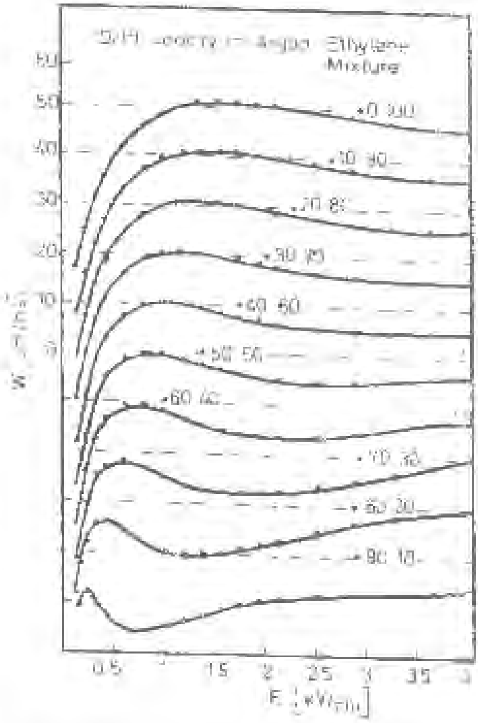

Figure 2.9: Drift velocity of electrons in an argon ethylene gas mixture, as a function of electric field [1, 2].

drift directions of the liberated electrons within the detectors. Both the "vertical" and "slanted" wire planes fall under the term vertical drift chamber as in both cases the drift direction of the liberated electrons is the same.

As the HDC is no longer being used, it will only be mentioned for the sake of completeness and not in much detail. All drift chambers, vertical, horizontal and slanted, were designed and commissioned by iThemba LABS.

Structurally, the drift chambers consist mainly of two high-voltage cathode planes with an anode signal-wire plane between them. A schematic view of the VDC is shown in figure 2.10.

As can be seen from the diagram, two mylar planes ($25\mu m$ thick) shield the interior wire-plane from atmospheric gases. The volume bounded by the two mylar planes is pressurised with a gas mixture consisting of 90% Ar and 10% CO_2. The two high-voltage cathode planes are constructed from two pieces of aluminium foil $27\mu m$ thick and separated by a distance of 16mm. When in operation, the cathode planes are kept at a constant negative voltage of

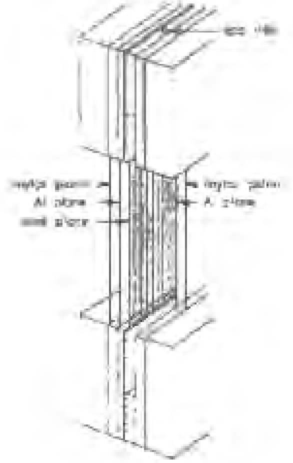

Figure 2.10: Schematic view of a VDC at iThemba LABS [19].

approximately −3800V. This MWPC configuration is the same in principle as the theoretical MWPCs described earlier, except in practice the cathode plane is kept at a constant negative voltage instead of the anode-wire plane being kept at a constant positive voltage.

The signal wire-plane of each VDC consists of 198 gold-plated tungsten signal wires each $20\mu m$ in diameter and spaced 4mm apart. To facilitate the drifting of charged particles (electrons) to the signal wires, the signal wire-plane is kept at a constant 0V potential. In between the 198 signal wires are a further 199 guard wires. These guard wires are constructed from $50\mu m$ thick gold plated tungsten, placed 4mm apart and kept at a constant negative voltage of ∼ 500V. These guard wires define cells 4mm in width associated with each signal wire [19]. If an electron drifts towards or is ionised near a guard wire, it will be deflected towards the zero-voltage signal wire nearest to it under the action of the Coloumb force.

The Horizontal Drift Chamber, HDC, mounted after VDC 2 and before the plastic scintillator detectors, is similar in concept, but slightly different in design. The HDC consists of 16 signal wires and 17 guard wires in a horizontal configuration. The operating voltages of the HDC are ∼ −2000V across the cathode plane and ∼ −1200V across the guard wires. It can be seen that the main difference between the VDC and HDC is the drift direction of electrons within the drift chamber. In the case of the VDC, the drift direction of an electron is perpendicular to the plane of signal wires while in the HDC the drift direction of an electron is along the plane of signal wires.

As stated earlier, the new MWPCs contain the original vertical anode-wire plane and an additional slanted anode-wire plane. The decision to implement a slanted wire plane stems from the fact that it yields high resolution vertical information in a detector comparable in size to the current VDCs. When designing the new slanted anode-wire plane, two primary factors were considered: Firstly, at what angle to the vertical should the slanted wires be placed? Secondly, given that the slanted wire-plane is positioned a distance behind the vertical wire-plane within the MWPC, how many wires are needed in the slanted wire-plane to ensure that all events collected from the vertical wire-plane are also collected in the slanted wire-plane [13]. The second factor is an important one as, for data to be considered valid, there must be a coincidence of detection across all four wire-planes (spanning the two MWPCs) as well as two paddle detectors, which provide timing information and will be discussed in more detail later.

The U-plane wire angle was calculated by way of a hit analysis [13]. Consider a particle incident on a detector whose wires are slanted at an angle of 45° to the vertical. The particles motion through the detector is shown in Figure 2.11, as well as the drift direction of ionised electrons:

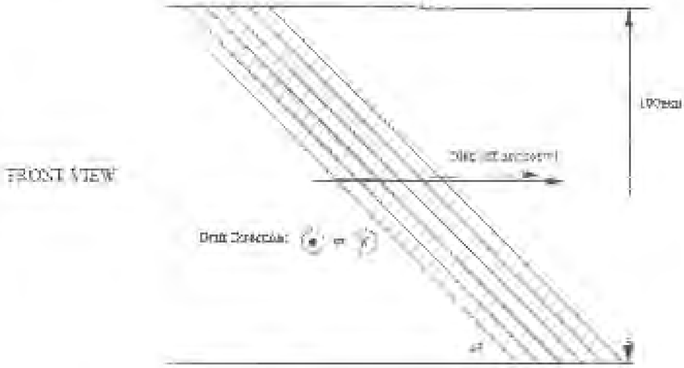

Figure 2.11: Front view of an incident particle's motion through a slanted wire-plane [13].

It is clear, from Figure 2.12, that the U-plane will function in exactly the same manner as the X-plane; the only difference being the number of wires that fire per event, assuming that the perpendicular wire-spacing is the same as that of the X-plane. To find out how many wires fire for various types of

Figure 2.12: Top view of an incident particle's motion through a slanted wire-plane [13].

events, a hit analysis was performed at iThemba LABS. The two trajectories depicted in the figure above are for two particles: one travelling horizontally and the other two degrees off horizontal.

From measurements carried out at iThemba LABS, it was determined that high dispersion plane events peak at six wires, while medium dispersion plane events peak at five wires [13]. As the medium dispersion plane is the more restrictive of the two, the hit analysis was performed for this case.

From calculations previously carried out by Dr F.D. Smit [31], the minimum and maximum focal-plane trajectory angles for particles in the medium dispersion plane were calculated to be 29.8 and 42.9 degrees respectively. The best approximation for the angle of the central ray was calculated to be 35.75°. Figures 2.13, 2.14 and 2.15 below illustrate the trajectories of three hypothetical incident particles with angles equal to the minimum, maximum and nominal trajectory angles respectively [13]:

Figure 2.13: Minimum medium dispersion plane particle trajectory [13].

From these figures it can be seen that the minimum angle particle trajectory causes seven wires to be fired. The maximum angle particle trajectory causes four wires to be fired and the nominal angle particle trajectory causes six wires to be fired within the existing VDC.

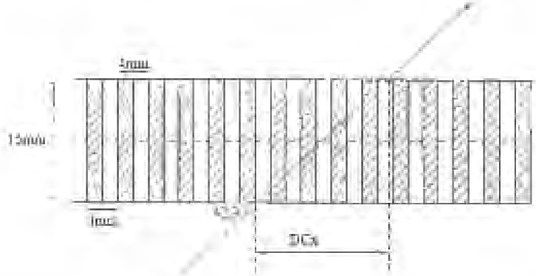

Figure 2.14: Maximum medium dispersion plane particle trajectory [13]

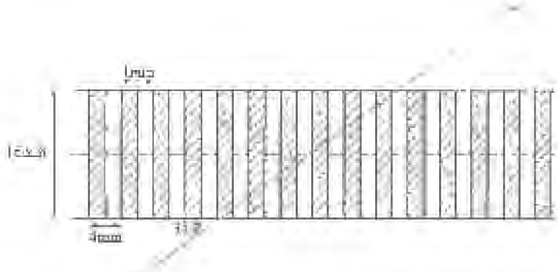

Figure 2.15: Nominal medium dispersion plane particle trajectory [13]

Figures 2.13, 2.14 and 2.15 assume that the width of the signal-wire cell, created by the guard wires, is half the signal-wire to signal-wire distance. This of course implies that the width of the guard-wire cell is half the guard-wire to guard-wire distance. Employing this assumption allows us to estimate the horizontal path size of an incident particle within the detector. This horizontal path is defined as the total horizontal distance which an incident particle travels within the detector for an event where n signal-wires and $n-1$ guard-wires fire. This definition also applies to detector events where n guard-wires and $n-1$ signal-wires fire. The total horizontal distance is denoted by the variable DC_{xn}, and is related to the number of wires that fire and to the spacing of those wires by the following formula [13]:

$$DC_{xn} = (n - \frac{1}{2}) \times wirespacing. \tag{2.5}$$

Making judicious use of the detector geometry, this horizontal distance can also be written in terms of the detector width and the angle that the incident particle makes with the focal-plane [13]:

$$DC_x = \frac{16mm}{\tan\left(\theta_{track}\right)} \tag{2.6}$$

Using equations (2.5) and (2.6) above allows us to estimate the number of wires that should fire for an event of any angle. For the purposes of a hit analysis, however, the most relevant angles are the minimum, maximum and nominal. The table below shows the horizontal distance that an incident particle travels inside the detector as well as the number of wires expected to fire for various possible angles of the slanted wire-plane [13]:

Particle track	DC_x	No. of wires (4mm spacing)	No. of wires (5.66mm spacing)	No. of wires (6mm spacing)
29.8°	27.9mm	6 or 7	4 or 5	4 or 5
35.9°	22.1mm	5 or 6	3 or 4	3 or 4
42.9°	17.2mm	4 or 5	2 or 3	2 or 3

The wire-spacing above refers to the horizontal distance between each of the signal (and therefore also guard) wires. The perpendicular distance, however, is kept at a constant 4mm. The 4mm perpendicular wire-spacing thus obviously corresponds to a standard VDC, while the 5.66mm perpendicular wire-spacing corresponds to a slanted wire-plane angle of 45° and the 6mm perpendicular wire-spacing corresponds to a slanted wire-plane angle of 41.8°.

To make adequate use of the slanted wire-plane, one has to ensure that at least three to four wires fire for the worst case event, which here corresponds to the maximum angle. To ensure that at least four wires fire for this event, the horizontal wire-spacing is calculated as:

$$\left(4 - \frac{1}{2}\right) \times wirespacing = \frac{17.2}{4 - \frac{1}{2}} = 4.91mm. \tag{2.7}$$

Knowing both the horizontal and perpendicular wire-spacing allows us to calculate the wire-plane angle using simple trigonometry. The perpendicular wire-spacing is known to be 4mm, resulting in a U-plane angle of:

$$\sin\left(\theta_{wireplane}\right) = \frac{4}{4.91}. \tag{2.8}$$

so that

$$\theta_{wireplane} = 54.5^{\circ}$$

.

Thus a wire-plane angle of at least 54.5° is needed to ensure that enough wires fire to create useable data in all cases.

2.5 Spanning the Entire X-plane

As mentioned previously, the second factor that was taken into account during the drift chamber construction was the horizontal size of the new U-plane. Consider the new wire-plane to be comprised only of full length wires and to be the same size as the original X-plane. It is clear in this scenario that there will be dead regions at the edges of the U-plane [13]. These dead regions interfere with the coincidence necessary for data acquisition. Figure 2.16 below depicts the situation.

From Figure 2.16 it can be seen that, if the new U-plane is the same size as the existing X-plane, all valid readings close to the edge of the X-plane will not register on the U-plane. This will force the data acquisition system to disregard data that would be considered valid in a detector with a larger slanted wire-plane.

To correct for this problem, the horizontal size of the U-plane must be larger than that of the X-plane. Assuming the previously calculated wire-plane angle of 54.5° and the detector geometry shown in the image below, we can calculate how much longer the U-plane must be.

From the detector geometry shown in Figure 2.16, it is clear that, to span the entire X-plane, the U-plane must be an additional [13]:

$$\frac{100mm}{\tan\left(54.4^{\circ}\right)} = 71.6mm \tag{2.9}$$

larger on either end of the existing X-plane. With a known horizontal wire-spacing of 4.91mm, this results in an extra 14 wires being needed on either side of the X-plane.

The above argument assumes that the centre of the U-plane is in exactly the same position within the detector as that of the X-plane. In reality, however,

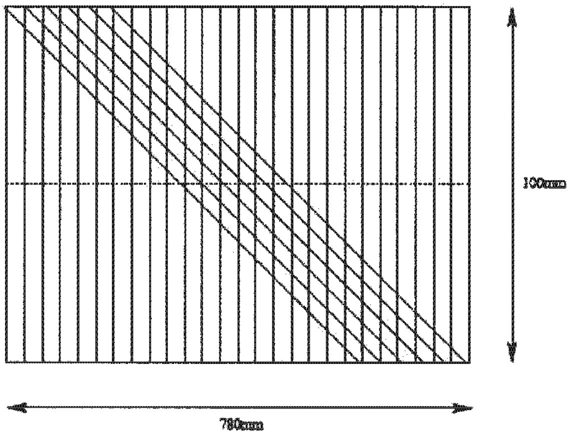

Figure 2.16: Wire-plane geometry of the iThemba LABS MWPCs [13].

the U-plane will be 16mm behind the X-plane. This distance is compensated for by a horizontal shift of [13]:

$$\frac{16mm}{\tan(35.75^{\circ})} = 22mm. \tag{2.10}$$

2.6 Other Components, TDCs and Paddle Detectors

Thus far we have considered only the two drift chambers in the focal-plane detector package. These two drift chambers do, however, depend primarily on two additional pieces of equipment to meet experimental needs, namely Time to Digital Converters, or TDCs, and Paddle Detectors. We begin with the paddle detectors.

2.6.1 The Paddle Detector

The very last components in the focal-plane detector package is a set of two plastic scintillator detectors each connected to two photomultiplier tubes. The rectangular plate of the plastic scintillator, when connected to the photomultiplier tube, resembles a bat or a paddle and hence the name.

The inner workings of the paddle detector, while well documented, will be included here for the sake of completeness. A plastic scintillator is understood to be a material which, when a charged particle passes through it, emits a photon. These photons usually fall into the 100 400nm wavelength range, which corresponds to the violet or ultra-violet range. This range implies that plastic scintillators are susceptible to background atmospheric radiation and explains why unshielded plastic scintillators often appear to be purple around the edges. To correct for this high susceptibility of plastic scintillator material to ambient light, the plastic scintillator paddles in the focal-plane detector package were light-proofed by wrapping them in black paper and the edges were secured with black tape. This ensures that no background light creeps into the scintillator material, which would compromise the readings.

Plastic scintillator materials are manufactured in many forms and from many substances. The paddle detectors in the focal-plane detector package of the K600 magnetic spectrometer are constructed from solid state scintillators, in this case BC-408 premium plastic scintillator manufactured by Bicron [32].

When a charged particle is incident on the plastic scintillator, it excites the electrons within to an energy level proportional to the energy of the incident charged particle. When the excited electrons de-excite, photons are emitted as the excited electrons return to their ground state energies. The photons produced, however, are too small in number to be easily detected. In addition to this the produced photons are unlikely to have a trajectory in the desired direction (towards the detector).

To ensure that these photons are directed towards the detector a light guide is used. The light guide simply provides a reflective medium which reflects photons towards the photomultiplier tube. To prevent the produced photons from escaping, the plastic scintillator material is wrapped in smooth white paper (located under the light-proofing), to ensure that the photons stay within the scintillator plate until they are scattered into the photomultiplier tube. Ensuring that the maximum number of produced photons reaches the detector is of great importance as each photon represents a reading and the detection of that photon is used to generate trigger information.

These few produced photons are still too few in number to be detected, however, and must therefore be increased in number until they can produce a detectable current. This amplification of the produced photons is facilitated by the photomultiplier tube.

The photomultiplier tube is a circuit element founded on the photoelectric effect. The photoelectric effect, which won Einstein the 1921 Nobel Prize, states that a photon with energy greater than the threshold energy of a metal may cause an electron to be ejected from that metal. A schematic diagram of the photomultiplier tube is shown in Figure 2.17.

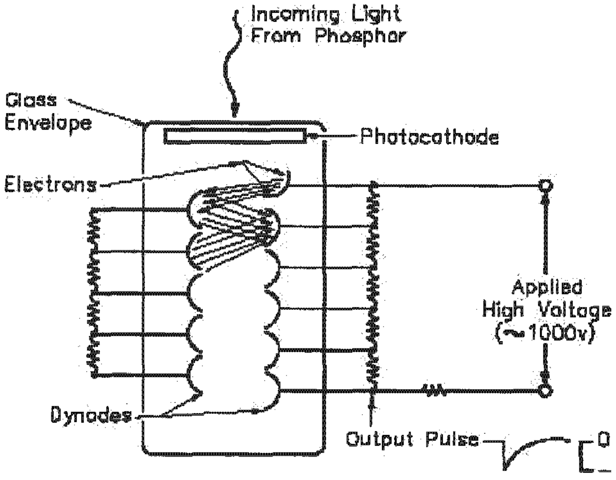

Figure 2.17: Schematic diagram of a photomultiplier tube containing 11 dynodes.

As can be seen from Figure 2.17, the top layer of the photomultiplier tube is a photocathode which ejects an electron when a photon, in this case from the plastic scintillator, is incident on it. This ejected electron then strikes a dynode, a circuit element which ejects multiple electrons when a single electron strikes it. The number of electrons ejected from the dynode is determined by the material from which the dynode is constructed as well as the energy of the incident electron.

The dynode is coated in a secondary emissive material which facilitates the ejection of multiple electrons from a minimum of one single incident electron. One dynode, however, is not enough to amplify the number of electrons to a detectable level. It is for this reason that most photomultiplier tubes contain a chain of $\sim$ 10 dynodes. The photomultiplier tubes at iThemba LABS contain 12 linear focused dynodes [32, 21].

Each dynode in the chain is held at a certain potential, relative to the other dynodes, to ensure that all secondary electrons are directed down the chain and towards the detector. As the secondary electrons are accelerated from dynode to dynode, they cause even more electrons to be ejected. These electrons in turn strike another dynode and cause additional electrons to be ejected until what started out as an undetectable $\sim$ 1 electron at the photocathode becomes an easily detectable 10^4 - 10^5 electron current at the terminal of the detector [27].

2.6.2 The Time to Digital Converter

The information generated by a MWPC must be extracted before it can be used in data acquisition. There are a number of possible ways to do this. The most standard method, however, is to consider each of the signal wires as its own detector with its own detector electronics [1]. The MWPCs at iThemba LABS are treated in this way. Each wire in the signal-wire plane is connected to a pre-amplifier which is in turn connected to a unique channel on a Time-to-Digital Converter (TDC) module. The role of the TDC is to obtain a time interval measurement in a digital format [1].

The time interval measurement is obtained by using a start signal to activate a scaler (an electronic device which stores accumulated data) which is set to count the number of oscillations of a clock oscillating at a constant frequency [1]. When the time interval to be measured draws to a close a stop signal is then sent to the scaler which, at this point, ceases to accumulate. Given the constancy of the oscillating clock, it follows that the value accumulated by the scaler will be proportional to the time interval between the start and stop signals.

The resolution of the TDC unit depends on the frequency of the internal clock used. The higher the internal clock frequency, the smaller the time interval measured.

The TDCs used at iThemba LABS are the V1190A and V1190B TDC modules developed by CAEN. The V1190A TDC module is single-unit sized VME 6U module that contains 128 independent time-to-digital conversion channels [18]. Each unit contains four high-performance TDC chips developed by CERN. The resolution of the V1190A TDC module can be set to 100, 200 or 800 *ps*.

The V1190B TDC unit is also a single-unit sized VME 6U module that contains 64 independent time-to-digital conversion channels and also shares most of the V1190A's feature set, excepting that the V1190B TDC unit contains only two high-performance TDC chips [18].

The high-performance TDC chips used in both the V1190A and B units is a general purpose time-to-digital converter, which contains 32 independent channels per chip. The chip can be programmed to detect the rising and/or falling edge of the input pulse.

The programming of both the V1190A and B units is facilitated by a micro-controller that implements a high-level interface to the user, which allows the user easy access to the functionality of the TDC unit while at the same time masking the raw TDC hardware. A block-diagram of the V1190A unit is shown in Figure 2.18.

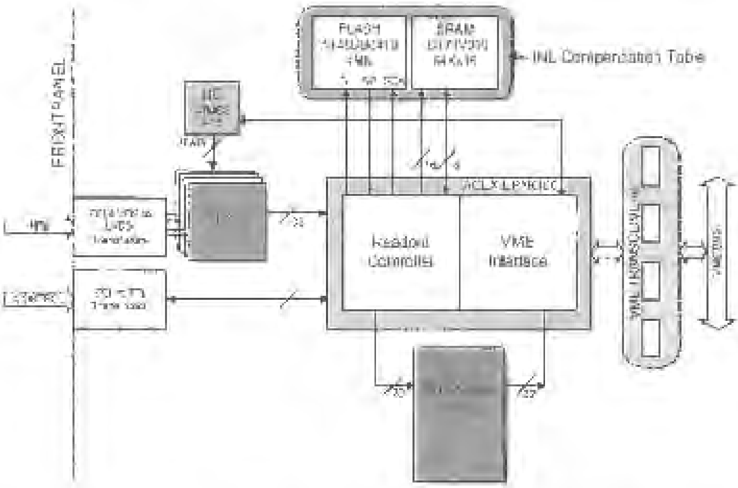

Figure 2.18. Block diagram of the V1190A TDC [18].

Chapter 3

Mathematical Methods for Data Analysis

Thus far we have the following information available to us: From the preamp electronics we know which wire, and therefore which cell, detected the ionised electrons. From the paddle detectors and TDCs we know the point in time at which the incident radiation arrived and we know the drift time of each of the ionised electrons.

3.1 Linear Least Squares Fit

Electrons are liberated along the path of the incident radiation only. Knowing which wire, or cell, the ionised electrons were detected at gives us horizontal or X information about the location of the incident radiation at a point in time, while knowing the drift time of each of the ionised electrons allows us to calculate vertical or Y information via the following relation [19]:

$$D_i = T(t_i), \tag{3.1}$$

where D_i is the vertical drift distance of the i^{th} ionised electron, t_i is the drift time of the i^{th} ionised electron and T is a Look Up Table (LUT) relating the drift time of the ionised electrons to their respective drift distances. This drift table is stored in an online database within the data acquisition software and will be dealt with in more detail later.

Let us assume, for the time being, that we now have two lists of information: one list containing X information of points along the path of the incident radiation and another list containing the corresponding Y information for each of the X points, calculated from the LUT. An example six wire event is shown in Figure 3.1 [13].

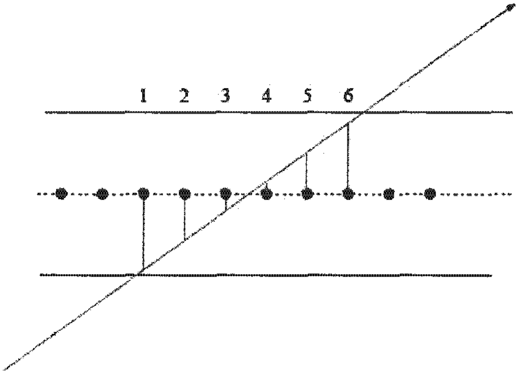

Figure 3.1: An example detector event where six wires fire.

From the figure it becomes clear that reconstructing the trajectory of the incident radiation entails calculating the best-fit curve for the X and Y data. The trajectory of the incident radiation will, in principle, be a straight line as there are no external forces acting on the particle this far down the beam line [19].

Mathematically, the vertical information, calculated from the LUT, of each point corresponds to the offset of that point from the straight line we wish to find. Logically the next step is to find the straight line whose parameters fit the recorded data best. One intuitive way of doing this would be to minimise the sum of the offsets. This, however, cannot be used as the function obtained from the absolute values of the offsets is discontinuous and, therefore, cannot be treated analytically [29]. Instead we minimise the sum of the squares of the offsets, which yields a function which is both continuous and differentiable. The sum of the squares of the offsets from n known data points, R, is given by the following formula [5]:

$$R^2 = \sum_{i=1}^{n} \left[y_i - f\left(x_i, a_1, a_2, a_3, \ldots, a_m\right)\right], \tag{3.2}$$

where y_i is the i^{th} experimental function value, x_i is the i^{th} experimental X datum and the a_j, where $j \in \{1 \ldots m\}$, are the function parameters to be fitted. Here

$$f\left(x_i, a_1, a_2, a_3, \ldots, a_m\right)$$

is the general function being fitted.

From the formula above it is clear that, if a judicious choice of the a_n is made, the value of R^2 will be small. If a perfect fit is obtained, then R^2 will be zero. Conversely, when R^2 takes on a minimum value, the a_m will provide the best-fit parameters. The condition for R^2 to be a minimum is [29, 5]:

$$\frac{\partial(R^2)}{\partial(a_i)} = 0, \tag{3.3}$$

for $i = 1, \ldots, n$. Looking at a straight line fit specifically, and thus setting

$$f(x_i, a, b) = a + bx_i,$$

yields the following:

$$R^2(a, b) \equiv \sum_{i=1}^{n} \left[y_i - (a + bx_i)\right]^2 . \tag{3.4}$$

Using equation (3.3) above to minimise R^2 gives

$$\frac{\partial(R^2)}{\partial a} = -2 \sum_{i=1}^{n} \left[y_i - (a + bx_i)\right] = 0, \tag{3.5}$$

$$\frac{\partial(R^2)}{\partial b} = -2 \sum_{i=1}^{n} \left[y_i - (a + bx_i)\right] x_i = 0. \tag{3.6}$$

Rearranging the above two equations:

$$na + b \sum_{i=1}^{n} x_i = \sum_{i=1}^{n} y_i, \tag{3.7}$$

$$a \sum_{i=1}^{n} x_i + b \sum_{i=1}^{n} x_i^2 = \sum_{i=1}^{n} x_i y_i. \tag{3.8}$$

Combining the above two formulae and solving for the parameters a and b yields a unique solution:

$$\begin{aligned} a &= \frac{\sum_1^n y_i \sum_1^n x_i^2 - \sum_1^n x_i \sum_1^n x_i y_i}{n \sum_1^n x_i^2 - \left(\sum_1^n x_i\right)^2}, & (3.9) \\ &= \frac{\bar{y} \sum_1^n x_i^2 - \bar{x} \sum_1^n x_i y_i}{\sum_1^n x_i^2 - n\bar{x}^2}, & (3.10) \end{aligned}$$

$$\begin{aligned} b &= \frac{n \sum_1^n x_i y_i - \sum_1^n x_i \sum_1^n y_i}{n \sum_1^n x_i^2 - \left(\sum_1^n x_i\right)^2}, & (3.11) \\ &= \frac{\sum_1^n x_i y_i - n\bar{x}\bar{y}}{\sum_1^n x_i^2 - n\bar{x}^2}, & (3.12) \end{aligned}$$

where

$$\bar{x} \equiv \frac{1}{n} \sum_{i=1}^{n} x_i$$

and

$$\bar{y} \equiv \frac{1}{n} \sum_{i=1}^{n} y_i$$

are the mean x and y values.

The correlation coefficient, r, is given by:

$$r = \frac{\sum_{i=1}^n (x_i - \bar{x})(y_i - \bar{y})}{\sqrt{\sum_{i=1}^n (x_i - \bar{x})^2 \sum_{i=1}^n (y_i - \bar{y})^2}} \qquad (3.13)$$

These parameters define the best-fit straight line for the data set of x_i,y_i. This best-fit line corresponds directly to the trajectory of an incident particle. The formulae for a and b calculated above are not ideal for use in computer programming and so the following variable substitutions are introduced [5]:

$$\begin{aligned} SS_{xx} &= \sum_{i=1}^{n} (x_i - \bar{x})^2, & (3.14) \\ &= \left(\sum_{i=1}^{n} x_i^2\right) - n\bar{x}^2, & (3.15) \end{aligned}$$

$$SS_{yy} = \sum_{i=1}^{n} (y_i - \bar{y})^2 , \tag{3.16}$$

$$= \left(\sum_{i=1}^{n} y_i^2 \right) - n\bar{y}^2, \tag{3.17}$$

$$SS_{xy} = \sum_{i=1}^{n} (x_i - \bar{x}) (y_i - \bar{y}) , \tag{3.18}$$

$$= \left(\sum_{i=1}^{n} x_i y_i \right) - n\bar{x}\bar{y}. \tag{3.19}$$

These variable substitutions reduce the equations for a,b and r to [5]:

$$b = \frac{SS_{xy}}{SS_{xx}}, \tag{3.20}$$

$$a = \bar{y} - b\bar{x}. \tag{3.21}$$

$$r = \frac{SS_{xy}}{\sqrt{SS_x SS_y}} \tag{3.22}$$

The errors associated with the calculated parameters were calculated to be [5]:

$$u(b) = \sqrt{\frac{\sum_1^n R_i^2}{n \sum_1^n x_i^2 - \left(\sum_1^n x_i\right)^2} \left(\frac{n}{n-2}\right)}, \tag{3.23}$$

$$u(a) = \sqrt{\frac{\sum_1^n R_i^2 \sum_1^n x_i^2}{n \left(n \sum_1^n x_i^2 - \left(\sum_1^n x_i\right)^2\right)} \left(\frac{n}{n-2}\right)}, \tag{3.24}$$

where $R_i = y_i - (a + bx_i)$

These formulae allow us to calculate the necessary properties of the incident radiation - namely the position, denoted here by x, and its associated error

$u(x)$, and the angle θ, and its associated error $u(\theta)$ - by a simple manipulation of the best-fit straight line. The equations for these variables are as follows:

$$\begin{aligned} x &= -\frac{a}{b}, \qquad (3.25) \\ \frac{u(x)}{x} &= \times\sqrt{\left(\frac{u\,(b)}{b}\right)^2 + \left(\frac{u\,(a)}{a}\right)^2}, \qquad (3.26) \end{aligned}$$

$$\begin{aligned} \theta &= \tan^{-1}(b), \qquad (3.27) \\ u(\theta) &= \frac{1}{1+b^2}. \qquad (3.28) \end{aligned}$$

At this point in the design phase it was deemed necessary to test the results of the line-fitting routine by examining the quantities derived from the fit, namely position and angle. The calculated values of position and angle were found to be of the correct order of magnitude but did not exhibit the numerical accuracy expected. It was reasoned that a numerical error manifest in the calculated values of position and angle most likely originated from the paramaters a and b.

What was found was that the information contained in the least significant bits of the paramaters a and b was being truncated, resulting in information being lost. This loss of information was attributed to computational rounding error.

3.2 Roundoff Error in Real Number Representation

Real number representation in computers is limited as each variable has a maximum allowed size, measured usually in *Bytes* [6]. It follows that each variable must also have a maximum allowed precision. Consider a pair of one byte, or 8-bit, binary variables with the following values:

$x = 11111111$, $y = 00000001$

Consider now a third 8-bit variable, say z, which is the sum of x and y:

$$\begin{aligned} z &= x + y, && (3.29) \\ z &= 100000000. && (3.30) \\ &= 00000000. && (3.31) \end{aligned}$$

As computer addition is calculated from the least to the most significant bit and only 8 bits are allotted to the variable z, it is clear that the leftmost bit would be lost by the above addition as the computer would have to truncate the variable to fit within its allotted variable size. In decimal terms, this would result in the following sum:

$$\begin{aligned} z &= 255 + 1, && (3.32) \\ &= 0. && (3.33) \end{aligned}$$

This type of rounding error is known as overflow error and is so termed because the most significant bit has flowed over and been lost to truncation [7]. On the other end of the spectrum, we also have what is known as underflow error. Consider the following three 4-bit variables: two (a,b) with all four bits to the right of the decimal point, constructed to represent a real number less than unity, and one (c) with all four bits to the left of the decimal point:

$$\begin{aligned} a &= .1111 && (3.34) \\ b &= .xxxx && (3.35) \\ c &= 0010. && (3.36) \end{aligned}$$

where $x = 0$ or 1.

If we now perform the following operation:

$$b = \frac{a}{c}, \qquad (3.37)$$

We obtain the result:

$b = 1111.$

However, as there are only four bits allotted to the variable b, the fifth bit is truncated. In decimal terms this results in the following erroneous quotient:

$$b = \left(\frac{15}{16}\right) \times \frac{1}{2}, \tag{3.38}$$

$$= \frac{15}{16}. \tag{3.39}$$

From the above explanation of underflow, it ought to be clear that, should two real numbers extremely close to each other be subtracted from one another, the result of that subtraction would either be heavily truncated or zero. Neither of these two scenarios is acceptable in a high precision experiment, where any limitations should be defined by the experimental setup.

Before programming an entirely different curve-fitting routine, there was one last test to be carried out. If the problem was indeed rounding error, then increasing the size of each variable should have, in theory, caused the calculated values of position and angle to have had an increased numerical accuracy. All floating point variables were converted to double floating point variables and the newly calculated values of position and angle were indeed found to a greater degree of accuracy.

Although the calculated values of position and angle were known to a greater degree of accuracy, this increase in precision was obtained at a far higher memory cost. This is clearly unacceptable and as a result a more robust line-fitting method was implemented [6] and is presented in the following section. The standard straight-line fitting routine was left in the data acquisition system as it could prove useful in the future.

3.3 A More General Straight Line Fitting Technique

If we assume the uncertainty associated with each measurement y_i, denoted here by s_i, to be known, and again assume that the values of the dependent variables, denoted here by x_i, are exact, then the χ^2 merit function can be used to measure the goodness-of-fit as follows:

$$\chi^2(a,b) = \sum_{i=1}^{n} \left(\frac{y_i - a - bx_i}{\sigma_i}\right)^2. \tag{3.40}$$

Again, we minimise the χ^2 function with respect to the two parameters a and b to find the best fit straight line:

$$\frac{\partial\chi^2}{\partial a} = -2\sum_{i=1}^{n}\frac{y_i - a - bx_i}{\sigma_i^2} = 0, \tag{3.41}$$

$$\frac{\partial\chi^2}{\partial b} = -2\sum_{i=1}^{n}\frac{(y_i - a - bx_i)\,x_i}{\sigma_i^2} = 0. \tag{3.42}$$

As before, we rewrite the individual sums in the above equations in a more readable form using the following definitions [6]:

$$S \equiv \sum_{1}^{n}\frac{1}{\sigma_i^2}, S_x \equiv \sum_{1}^{n}\frac{x_i}{\sigma_i^2}, S_y \equiv \sum_{1}^{n}\frac{y_i}{\sigma_i^2}, S_{xx} \equiv \sum_{1}^{n}\frac{x_i^2}{\sigma_i^2}, S_{xy} \equiv \sum_{1}^{n}\frac{x_i y_i}{\sigma_i^2} \tag{3.43}$$

Substituting these sums into equation (3.42) above yields two equations for two unknowns, much the same as the previous method:

$$aS + bS_x = S_y, \tag{3.44}$$

$$aS_x + bS_{xx} = S_{xy}. \tag{3.45}$$

The solution to these two equations is:

$$a = \frac{S_{xx}S_y - S_x S_{xy}}{SS_{xx} - (S_x)^2}, \tag{3.46}$$

$$b = \frac{SS_{xy} - S_x S_y}{SS_{xx} - (S_x)^2}. \tag{3.47}$$

The formulae calculated above still have the same inherent flaw as the previous ones: they still rely on the subtraction of two numbers which, by design, are very close together. The correction for roundoff error works by altering the data set of the dependent variable, in this case the x_i. The correction is performed as follows:

$$t_i \equiv \frac{1}{\sigma_i}\left(x_i - \frac{S_x}{S}\right), \tag{3.48}$$

$$S_{tt} = \sum_{i=1}^{N} t_i^2. \tag{3.49}$$

Substituting the above two equations into equation (3.42) yields [6]:

$$b = \frac{1}{S_{tt}} \sum_{i=1}^{N} \frac{t_i y_i}{\sigma_i}, \tag{3.50}$$

$$a = \frac{S_y - S_x b}{S}. \tag{3.51}$$

with the following uncertainties:

$$\sigma_a^2 = \frac{1}{S}\left(1 + \frac{S_x^2}{S S_{tt}}\right), \tag{3.52}$$

$$\sigma_b^2 = \frac{1}{S_{tt}}. \tag{3.53}$$

The σ_i are not measured explicitly at iThemba LABS. However, seeing as though all drift chambers and TDCs are identical, the σ_i can be assumed to be the same. Employing this assumption allows us to make a few changes to the formulae above, namely:

$$t_i = \frac{1}{\sigma_i}\left(x_i - \frac{S_x}{n}\right), S_x = \sum_1^n x_i, S_y = \sum_1^n y_i, S_x x = \sum_1^N x_i^2, S_x y \equiv \sum_1^N x_i y_i. \tag{3.54}$$

These equations, by direct substitution, yield:

$$\begin{aligned} b &= \frac{1}{S_{tt}} \sum_{i=1}^{n} t_i y_i & (3.55) \\ a &= \frac{S_y - S_x b}{n} & (3.56) \\ \sigma_a^2 &= \frac{1}{n}\left(1 + \frac{S_x^2}{S S_{tt}}\right) & (3.57) \\ \sigma_b^2 &= \frac{1}{S_{tt}} & (3.58) \end{aligned}$$

These parameters completely define the trajectory of the incident radiation and, as before, the necessary particle information is calculated as follows:

$$\begin{aligned} x &= -\frac{a}{b}, & (3.59) \\ u(x) &= \sqrt{\frac{\sigma_a}{b^2} + \frac{\sigma_b a^2}{b^4} - \frac{2cov(a,b)a}{b^3}} \times \sqrt{\frac{\chi^2}{(n-2)}}, & (3.60) \end{aligned}$$

where $cov(a, b)$ is the covariance of a and b, and χ^2 is the merit function used to find the best-fit parameters. These two quantities are given by:

$$\begin{aligned} cov(a,b) &= -\frac{S_x}{n S_{tt}}, & (3.61) \\ \chi^2(a,b) &= \sum_{i=1}^{n} (y_i - a - b x_i)^2 . & (3.62) \end{aligned}$$

The angular information is given by:

$$\begin{aligned} \theta &= \tan^{-1}(b), & (3.63) \\ u(\theta) &= \frac{1}{1+b^2}. & (3.64) \end{aligned}$$

This final set of equations is the one in use in the data acquisition system. It is worth noting, however, that, should the errors associated with the vertical information, σ_i, be measured through the installation of new electronics or rendered dependent on wire number, then the data acquisition system would have to be altered to use the above method.

Chapter 4

Application of Curve-Fitting Techniques to the VDCs at iThemba LABS

4.1 Trajectory Reconstruction in the X-plane

Explained in the previous chapter was a robust method by which a straight line could be fitted to a set of n experimental data points whose dependent, or x, variable values are known exactly and whose independent, or y, variable values have either a known error, denoted by σ_i, or an unknown error that can be assumed to be independent of the y data.

The applications of this line-fitting algorithm, however, are non-trivial and merit some explanation. As previously stated, the signals registered by the data acquisition electronics, namely the TDCs and paddle detectors, arrive at a front-end processing crate unit utilising the CAMAC standard. This front-end system in turn strips off control bits and performs other experimenter-defined housekeeping tasks, and then passes all collected data to the MIDAS analyser module in the form of an internal data structure known as a bank [20]. These so-called banks and their proper usage will be discussed in more detail later. For the purposes of this chapter, let us assume, once again, that all data arriving in the MIDAS bank consists of two lists containing x information (or wire number) and y information (drift distance). A hypothetical six wire event is shown in Table 4.1.

As stated previously, each drift chamber consists of two wire-planes: one

Table 4.1: A hypothetical six wire event

x (Wire Number)	y (Drift Distance)
x_1	d_1
x_2	d_2
x_3	d_3
x_4	d_4
x_5	d_5
x_6	d_6

vertical and one at an angle of 54.5° to the vertical. As the slanted wire-plane calculations depend on values calculated from the vertical plane, the vertical wire-plane will be considered first.

Suppose the event under consideration resulted from a trajectory as in Figure 4.1. It is reasonable to assume that the first and last drift distances are of opposite sign as the straight line along which they fall intersects the focal-plane. However, it must be noted that there is an ambiguity in the sign of the smallest drift distance [30].

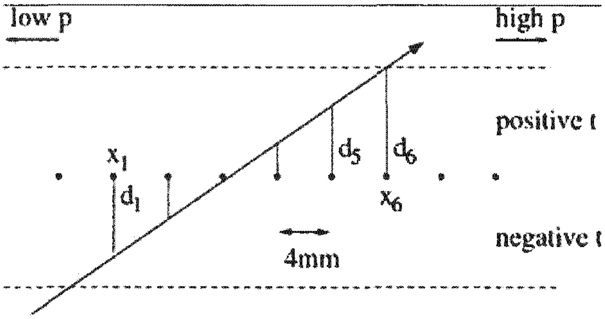

Figure 4.1: A six wire detector event with liberated-electron drift paths [30].

There are two immediately obvious ways to correct for this sign ambiguity. One way would be to ignore the smallest drift distance and fit the straight line to one fewer data points. This causes problems, however, as the curve-fitting routines described above require at least three wires to fire per event or, put another way, the curve-fitting methods require at least three points to fit a straight line. Therefore, ignoring the smallest drift distance renders perfectly good three wire events useless. [1]

The second option for correcting the sign ambiguity of the smallest drift distance would be to assume a sign and proceed with the line-fitting. As stated above, the line-fitting routine used makes use of the χ^2 merit function as a goodness-of-fit test. Once the line-fitting routine has been employed to fit the straight line, the goodness of fit metric is stored. A second straight line would then be fitted to the same data, but this time using the opposite sign of the smallest drift distance. The goodness-of-fit metric resulting from the second straight line fit is then also stored.

Clearly, whichever straight line possesses the lower value of the χ^2 merit function is the straight line which fitted the data better [8]. It therefore stands to reason that the straight line which possesses the higher χ^2 must have fitted the data worse and is discarded. This method was implemented as it allows for greater accuracy in measurement.

The above discussion is incomplete, as whichever curve-fitting method is used, the drift distance data set must be altered. As stated earlier, the electronics register the total drift time of each of the ionised electrons. The drift distances associated with these drift times are then retrieved from a look up table.

As all drift times recorded by the timing electronics are inherently positive, so too are all of the drift distances retrieved from the look up table. This is a problem as Figure 4.1 above clearly shows that some of the ionised electrons drift in the positive direction and some in the negative direction. The pattern is quite simple: All ionised electrons which arrive before the electron with the minimum drift distance must have their signs made negative, while all those arriving after the ionised electron with the minimum drift distance must have their signs left positive.

Thus a complete algorithm for calculating the trajectory of an incident particle of radiation in the focal plane, assuming MIDAS data banks populated with wire number and drift distances only, would look as follows:

- Isolate the electron with the minimum drift distance.
- Set the signs of all drift distances before the minimum to negative.
- Assume the sign of the minimum drift distance to be positive.

---

[1] The requirement of at least three data points by the curve-fitting algorithm stems from the fact that a straight line will always pass through two points without error.

- Use the curve fitting method described above to calculate the best-fit parameters a,b and χ^2.
- Set the sign of the minimum drift distance to negative.
- Use the curve fitting method described above to calculate the best-fit parameters a_2,b_2 and χ_2^2.
- Compare the values of χ^2 and χ_2^2. If $\chi^2 < \chi_2^2$, then the parameters a,b describe the best-fit straight line. Otherwise, the parameters a_2,b_2 describe the best-fit straight line.

Once the parameters for the best-fit straight line have been calculated, the necessary incident particle information, such as position and angle in the focal-plane and their associated errors, can be calculated from formulae (3.59), (3.60), (3.63), (3.64) above.

The units of the position of the incident radiation, calculated from formula (3.59) above, are worth considering. As stated above the data available to the fitting routine at this point are two lists: one list containing the numbers of the wires that fired and another list containing the corresponding drift distances. It therefore stands to reason that all positions calculated in the vertical wire-plane and in all other wire-planes are in terms of wire number.

As an example consider the position of a hypothetical incident particle the value of which was calculated to be 5.5. This result is interpreted as follows: the position of an arbitrary incident particle was found to be 5.5 wires, i.e. the particle crossed the focal-plane exactly midway between wires 5 and 6. Should the experimenter require the position of the incident radiation along the drift chamber in units of millimetres or metres, then the position determined from the straight line fit would have to be multiplied by the horizontal wire-spacing. In the case of the vertical wire-pane, this wire-spacing would be 4mm, and in the case of the slanted wire-plane, the wire-spacing would be 4.91mm [13].

4.2 Trajectory Reconstruction in the U-plane

Making use of the vertical wire-plane, we have reconstructed the trajectory of the incident radiation in the focal-plane. To obtain the trajectory of the incident radiation in the plane perpendicular to the focal-plane, we must consider the slanted wire-plane.

For the first part of the calculation the wire-plane angle can be ignored and the slanted wire-plane is treated as a vertical wire-plane. A straight line is fitted to the wire number data and unaltered drift distances to produce a position in terms of wire-number along the slanted wire-plane.

The same problems are encountered with the above curve-fitting procedure as were encountered when reconstructing the trajectory in the focal-plane. The sign of the smallest drift distance is also ambiguous and, as before, all drift distances occurring before the minimum drift distance must be made negative. The solution to the sign ambiguity of the minimum drift distance is resolved in the same manner: Two straight lines are fitted to the data, one straight line assuming a negative minimum drift distance and a second straight line assuming a positive minimum drift distance. As before, the χ^2 merit function is used as a goodness-of-fit test and the straight line resulting in the lower value of the χ^2 function is taken to be the best-fit straight line.

Utilising the information above, the vertical position in the focal-plane can be calculated as follows [13]:

Consider the two geometrical diagrams of the wire-planes inside each drift chamber depicted below [32]:

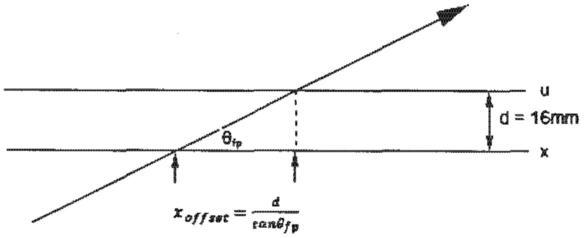

Figure 4.2: Top-down view of one of the new detectors at iThemba LABS. Both the X and U-planes are shown as well as the trajectory of an incident particle passing through the detector. The angle, θ_{fp}, refers to the angle at which the incident particle crosses the focal-plane, d is the distance between the vertical and slanted wire-planes within the new detector and x_{offset} is the distance between the horizontal positions in the vertical and slanted wire-planes.

From figures 4.2 and 4.3 it follows that:

$$AB = x - AD, \tag{4.1}$$

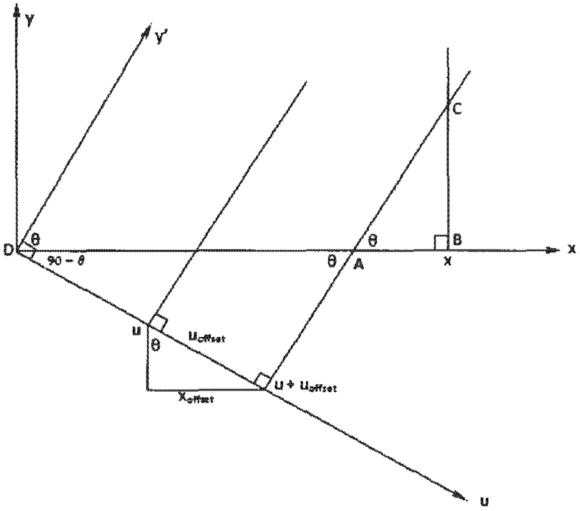

Figure 4.3: This figure illustrates the internal geometry of the new detectors used to calculate vertical position information. The angle θ refers to the slanted wire-plane angle, and u_{offset} is the distance between the vertical positions in the vertical and slanted wire-planes.

$$\begin{aligned}
\sin(\theta) &= \frac{u + u_{offset}}{AD}, && (4.2)\\
\Rightarrow AB &= x - \frac{u + u_{offset}}{\sin(\theta)}, && (4.3)\\
\tan(\theta) &= \frac{BC}{AB}, && (4.4)\\
\Rightarrow BC &\equiv y = AB\tan(\theta), && (4.5)\\
\sin(\theta) &= \frac{x_{offset}}{u_{offset}}, && (4.6)\\
\Rightarrow u_{offset} &= \frac{x_{offset}}{\sin(\theta)}, && (4.7)\\
&= \frac{d}{\sin(\theta)\tan(\theta_{fp})}, && (4.8)\\
\Rightarrow y &= \left(x - \frac{u + u_{offset}}{\sin(\theta)}\right)\tan(\theta), && (4.9)\\
y &= \left(x - \frac{u + \frac{d}{\sin(\theta)\tan\left(\theta_{fp}\right)}}{\sin(\theta)}\right)\tan(\theta). && (4.10)
\end{aligned}$$

$$y_1 = x_1 \tan(\theta) - \frac{u_1}{\cos(\theta)} - \frac{2d}{\sin(2\theta)\tan(\theta_{fp1})}. \tag{4.11}$$

Similarly for the y position in the second drift chamber we have:

$$y_2 = x_2 \tan(\theta) - \frac{u_2}{\cos(\theta)} - \frac{2d}{\sin(2\theta)\tan(\theta_{fp2})}, \tag{4.12}$$

where x_1 and x_2 are the positions in the focal-plane determined from the first and second vertical wire-planes, or the $X1$ and $X2$ planes, respectively. The angle θ corresponds to the slanted wire-plane angle, in this case 54.5°, and θ_{fp1} and θ_{fp2} correspond to the angles at which an incident particle crosses the focal-planes in the first and second detectors respectively. The distance d is the perpendicular distance between the two wire-planes within each detector.

The formulae above complete the trajectory reconstruction of the incident radiation both in the focal-plane and also in the plane perpendicular to the focal-plane. It is still necessary to know, or at least to estimate theoretically, how accurate our determination of the position actually is. To determine this position accuracy we refer to an article on drift chambers by [16].

4.3 Error in Position Determination

In Figure 4.1 a typical six-wire VDC event is illustrated. As there are no external forces acting on the incident radiation downstream of the spectrometer, the trajectory of the radiation is described by a straight line. This straight line geometry dictates that the particle trajectory should be at a constant angle on both sides of the wire-plane. Thus the two gradients, as calculated on both sides of the wire-plane, should be equal in magnitude, so that [13, 16]:

$$\frac{(d_{t1} - d_{t2})}{wirespacing} = \frac{(d_{t6} - d_{t5})}{wirespacing}, \tag{4.13}$$

where d_{tx} denotes the drift distance of wire x retrieved from the look up table using drift time t. In reality, however, this is not exactly the case and what results is a Gaussian distribution centered about zero. The deviation of the Gaussian distribution is given by [13]:

$$\sigma_D = (d_{t1} - d_{t2}) - (d_{t6} - d_{t5}) \tag{4.14}$$

This deviation is related to the standard deviation of the drift distance through the following formula [13]:

$$\sigma_D = 2\sigma_{drift-distance}. \tag{4.15}$$

If we now assume that the standard deviations of the drift distances are independent of wire-number, i.e.

$$\sigma_{drift-distance} = \sigma_{d_{t1}} = \sigma_{d_{t2}} = \sigma_{d_{t5}} = \sigma_{d_{t6}}, \tag{4.16}$$

then the accuracy in position determination, denoted σ_{pos}, is given by [9]:

$$\begin{aligned} FWHM_{pos} &= 2.35\sigma_{pos}, &(4.17)\\ &= 2.35\frac{\sigma_{drift-distance}}{\sqrt{n}}, &(4.18)\\ &= 2.35\frac{\sigma_D}{2\sqrt{n}}. &(4.19) \end{aligned}$$

where n is the number of wires used to calculate the particle's position. Some typical values for these variables taken from a (d, d') experiment at an energy of 46MeV are as follows [13]:

$$\begin{aligned} \sigma_{drift-distance} &= 0.2mm, &(4.20)\\ FWHM_{pos} &= 0.08mm. &(4.21) \end{aligned}$$

The above calculations determine the accuracy of position measurement in the X-plane only. To calculate the expected accuracy in the U-plane, we begin by assuming a typical event. Consider an arbitrary wire chamber event where five wires fire in the X-plane and 4 wires fire in the U-plane [13]. In addition to this assume:

$$\begin{aligned} \sigma_{drift-distance-X} &= 0.2mm, &(4.22)\\ \sigma_{drift-distance-U} &= 0.4mm. &(4.23) \end{aligned}$$

The value of $\sigma_{drift-distance-U}$ is purposefully chosen to be conservatively large so that the value obtained for $FWHM_{pos}$ is also conservatively large [13]. Substituting both values of $\sigma_{drift-distance}$ shown above into equation (4.19) yields the following [13]:

$$\begin{aligned} FWHM_X &= 2.35\frac{\sigma_D}{2\sqrt{n}}, && (4.24)\\ &= \frac{2.35 \times 0.4}{2\sqrt{5}}, && (4.25)\\ &= 0.21mm, && (4.26) \end{aligned}$$

and similarly for $FWHM_U$ we have:

$$FWHM_U = 0.42mm. \tag{4.27}$$

We now have the errors associated with the wire-number calculation in both the X and U planes for a typical event where five wires fire in the X-plane and four wires fire in the U-plane. Unlike the X-plane, however, the result of line-fitting in the U-plane does not yield position information directly, but rather the wire-number on the slanted wire-plane at which the incident particle was detected. The desired vertical position can then be inferred using equation (4.11) or (4.12).

Hence the value of $FWHM_Y$ must be calculated from the values of $FWHM_X$ and $FWHM_U$, in conjunction with the following altered form of equation (4.11) above modified for error propagation [13]:

$$FWHM_Y^2 = FWHM_X^2\left(\tan^2\theta_U + \frac{16^2 \times 2}{d^2 \times \sin^2\theta_U\cos^2\theta_U}\right) + \frac{FWHM_U^2}{\cos^2\theta_U}. \tag{4.28}$$

Assuming that the detectors are placed 200mm apart, $FWHM_Y$ is calculated to be:

$$FWHM_Y = 0.43mm. \tag{4.29}$$

With a less conservative estimate of $\sigma_{drift-distance-U} = 0.2\text{mm}$, $FWHM_Y$ is calculated as [13]:

$$FWHM_Y = 0.235mm. \tag{4.30}$$

Chapter 5

The Customised Analyser

5.1 The MIDAS Data Acquisition System

The Maximum Integrated Data Acquisition System (MIDAS), a data acquisition system under the Gnu Public License (GPL), is used in medium-scale nuclear and particle physics experiments. Developed in tandem by the Paul Scherrer Institute in Switzerland and TRIUMF in Canada [20], the system is essentially a collection of libraries, which facilitate the transport of experimental data between various computing hardware and software platforms, and also provides a means of data logging and overall system management [20].

MIDAS is comprised mainly of the following components or modules:

- A buffer manager to control data flow and message passing between all modules of the Data Acquisition System (DAQ).
- A message system to create and interpret the meaning of messages sent and received by the buffer manager.
- An Online Database (ODB) which stores information such as system and hardware settings as well as all other relevant experimental data.
- A MIDAS server which allows experiments to be controlled remotely via Remote Procedure Call (RPC) functions.
- A frontend module which allows all experimental equipment to be registered within the MIDAS framework and also provides a means of reading and storing all data collected by the registered equipment. This

data is then organised into a known format, known as a bank, and is then passed to the buffer manager.

- A data logger module which receives data from the buffer manager and stores that data to disk, magnetic tape or another computer via FTP.

- An analyser module which allows the experimenter to define his or her own custom application for performing data analysis on all recorded event data. Such analysis may include trajectory reconstruction, beam statistics or various histograms displayed by third party software. Customisation of the MIDAS analyser formed the bulk of this project and will be discussed in more detail later.

- A run control module which allows the experimenter to access the ODB to alter the current state of the DAQ. Such states refer to the operational status of the DAQ and include running, paused and stopped.

- A slow control system which allows the user to control hardware modules, such as magnets or other frontend equipment, via the online database.

- A history system. In addition to ordinary event data logging routines MIDAS provides a means of storing slow control data as well as any periodic events to disk. These events can then be easily and quickly retrieved from the ODB.

- An alarm system which, when triggered by a user-defined alarm trigger, allows the experimenter to log the alarm message to the experiment log file or interrupt data acquisition.

- An electronic logbook which allows the experimenter to store any relevant experimental information. The electronic logbook also allows the user to convert stored experimental logs into a form publishable over the internet.

5.2 The MIDAS Analyser

The MIDAS analyser module is a collection of files which allow the experimenter access to all acquired data either online during data acquisition or offline in replay mode [20]. The MIDAS analyser module is made up of the following files:

- "experim.h" : A header file which defines the ODB structure.
- "analyser.c" : This module is the core of the analyser and allows the user to define the structure of the data banks as well as the analyser and the online database. In addition, the analyser also provides the user with entry points into the MIDAS framework by means of user-programmable BEGIN OF RUN and END OF RUN functions.
- "adccalib.c" : An analysis module designed to take in ADC calibration data.
- "adcsum.c" : This file is used to store accumulated ADC data.
- "scaler.c" : A module used to store information from the scaling equipment.

MIDAS also allows the experimenter to program his or her own independent analyser module in an external file, provided that the user module is correctly registered within the MIDAS framework. Such an external analyser module was created and named "f-plane.c". As the name suggests, this file was responsible for all calculations carried out on focal-plane data. Such calculations include the trajectory reconstruction described previously as well as all histograms derived from raw and trajectory data.

In order to provide a more flexible framework for data analysis, MIDAS employs a unique multi-stage design. All incoming measured raw events are passed through several stages in the analyser module, each stage having a specific goal or task. Each separate stage has the ability to read any part of an event, perform arbitrary calculations on that event data and then add the results of the analysis back to the event. This multi-stage concept is depicted in Figure 5.1.

The banks referred to in Figure 5.1 above may be interpreted as internal MIDAS meta-variables used for data storage. The most simplified view of one such meta-variable is considered to be an array with first element equal to the number of entries in the array, say n, and the remaining $n-1$ elements equal to the data for a particular event.

This multi-stage design proves useful as, should any two calculations have intermediate results in common, those intermediate results may be written to a bank and then recalled in the later calculation without the need for recalculation. The most obvious example of this can be seen in Figure 5.1. In stage two of the hypothetical analysis above, the raw ADC data is calibrated

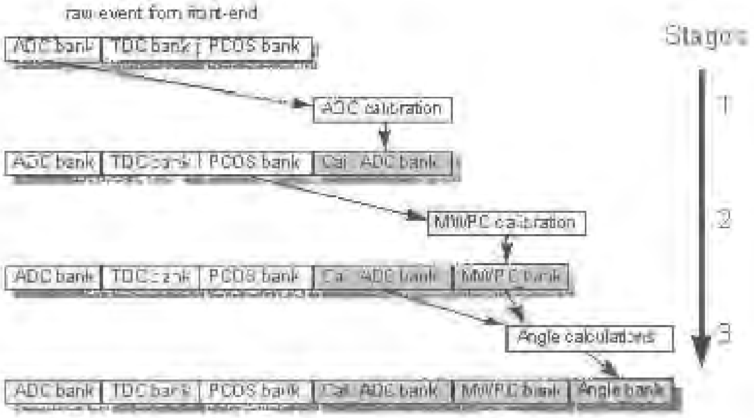

Figure 5.1: Schematic representation of the MIDAS multi-stage concept [20].

in some way and that calibrated data is stored in the Cal. ADC bank. Any subsequent stage in the analysis that requires calibrated ADC data, such as calculating the angle data, now has access to the Cal. ADC bank without the need to recalibrate.

5.3 The Customised MIDAS Analyser

As mentioned in §5.2, the first step in creating an analyser which is designed to work with the MIDAS data acquisition system is to register that analyser within the MIDAS software framework, so that MIDAS itself is aware that the experimenter wishes to use his or her own custom analyser. This registration is accomplished with the following line of code that was added to the module declaration portion of "analyzer.c":

```
extern ANA_MODULE focal_plane_module;
```

To complete the module registration process, the following line of code was added to the trigger module structure in the module declaration section of "analyzer.c":

```
&focal_plane_module;
```

The name used in module registration must correspond to the name defined in the module declaration portion of the actual customised module itself. Thus one cannot name ones module x within the module file and then register it as y within the analyser. In addition to this module registration, the custom module must also adhere to the existing MIDAS structure, i.e. there must exist certain methods within the module otherwise MIDAS will not run it, even if it is registered within "analyzer.c". The list of these mandatory methods is shown in Table 5.1.

Method Name	MIDAS Purpose
focal_event	Method to gain entry to MIDAS event data.
focal_bor	User-specific code to be executed at the beginning of an experimental run.
focal_eor	User-specific code to be executed at the end of an experimental run.
focal_init	User-specific code intended to initialise data structures.

Table 5.1: Mandatory methods in the MIDAS analyser.

Having ensured that MIDAS would use the custom analyser, "f-plane.c", and that the file contained all necessary methods expected by the MIDAS framework, construction of the program flow and methods of data storage were then considered. Of primary importance during the planning stages of the analyser was the balance between code abstraction and execution speed. In the field of computer science, the term abstraction refers to both the concept and methodology of factoring out unnecessary information so that fewer, more important, details may be considered [10].

As an example of the important role abstraction plays in programme design, consider the following short program, written in pseudo-code, designed to simulate a two step random walk:

```
x = random(0,1)
If x < 0.5 then go left
If x >= 0.5 then go right
x = random (0,1)
If x < 0.5 then go left
If x >= 0.5 then go right
```

The computer programme above is optimal in terms of calculation speed. However, should a twenty step random walk be required, it is obvious that the design of the programme above would soon become inconvenient; both to read and to maintain. The above program could be re-written in the following way:

```
random_min = 0
random_max = 1
p = 0.5
for i = 1 to 2 DO
x = random(random_min,random_max)
if x < p go left
if x >= p go right
```

Now the abstraction becomes clear. It is now obvious to the user what the goal of the programme is and how the solution is implemented. We have abstracted all numerical values from the programme and replaced them with meaningful variables. We have also removed the need to add many lines of code for more steps by looping the process. The resulting code is neater and more easily maintainable by another human being. Computationally, however, the second programme is less efficient. The addition of the loop means that the computer must keep track of an extra variable, namely the looping variable, and alter its value appropriately. In addition, the variable names must be resolved and the appropriate numerical values inserted before any calculations can be performed. The latter is usually handled by the compiler and does not affect the execution speed much.

Applying the principle of abstraction to the MIDAS analyser implies that all computationally-intensive tasks, such as data sorting, merging and manipulation, should be done as few times as possible and that each of these tasks should have as small an execution time as is reasonably possible. This principle was adhered to throughout all stages of the analyser design.

5.4 Analyser Program Flow and the Explanation Thereof

5.4.1 Reading and Manipulating Data from the ODB

As mentioned in §2.6.2, all wires in the anode wire-plane are treated as separate detectors, each with their own electronics. Each wire is connected to a unique channel on one of a number of CAEN V1190 TDC modules. These TDC modules each contain 128 independent channels [18] and, since there are 208 wires per wire-plane, it follows that each wire-plane would require at least two TDC modules.

These TDC modules do not necessarily have to be connected in any physically meaningful manner. At first glance one might think that the first wire in the first wire-plane of the first detector would be connected to the first channel of the first TDC module and the second wire in the first wire-plane of the first detector would be connected to the second channel of the first TDC module and so on. This setup, however, does not allow experimenters to alter the physical TDC channel connections without having to alter the data acquisition system code as well.

To solve this problem the detectors at iThemba LABS retrieve the TDC channel to wire-number mapping information from an online database. This allows experimenters to physically alter the TDC channel connections without having to alter the data acquisition software, provided the online database is correctly updated. This method of mapping the detector wire number to its corresponding TDC channel number proves useful in the event of one or more TDC channels failing.

The online database entries specific to an experimental run are stored in the same file used to store the event data and the online database is automatically updated when an experimental run file is loaded. This allows the data acquisition system programmers easy access to an accurate and constantly updated wire number map.

The code fragment used to access the online database is as follows:

```
/* open ODB structures */
cm_get_experiment_database(&hDB, NULL);
db_find_key(hDB, 0, "/Equipment/WireChamber/Settings", &hKey);
if (db_open_record(hDB, hKey, &WireChamberSettings_focal
```

```
, sizeof(WIRECHAMBER_SETTINGS), MODE_READ, NULL, NULL)
!= DB_SUCCESS)
{
cm_msg(MERROR, "analyzer_init",
"Cannot open \"/Equipment/WireChamber/Settings\" tree in ODB");
exit(1);
}
for(i=0;i<MaxWire_focal;i++)
{
module=i/128;
WireNum2Module_focal[WireChamberSettings_focal.channel2wire[i]]
=module;
Channel2Wire_focal[i]
= WireChamberSettings_focal.channel2wire[i];
}
db_close_record(hDB,hKey);
}
```

This code fragment searches the online database directory structure for the settings section and retrieves the database entries which map the TDC channel data to wire number data, namely `channel2wire`. The resulting array (`Channel2Wire\_focal`) is then used in the following manner:

```
Wire_number = Channel2Wire_focal[TDC_Channel_Number];
```

The second array populated in the database code fragment (`WireNum2Module`) is used to discern to which TDC module a wire of a given number is connected. As there are 128 channels per TDC module [18], it follows that the module number to which a given signal-wire is connected is simply the wire number itself divided by 128 with the decimal component of the quotient truncated. The wire number to module map is used in a similar manner to the wire number to channel map:

```
Module_number = WireNum2Module[Wire_number];
```

This allows the analyser module to easily convert TDC channel data to signalwire and module number data.

5.4.2 Locating the TDC Data Bank

Locating the TDC data bank is a relatively simple process involving just one method call. The method in question is the MIDAS-provided "*bk_locate*()" [20]. The correct usage of the locate method is as follows :

```
int bank_size = bk_locate(pevent, "TDC0", &ptdc);
```

The locate method above requires three arguments as input and returns an integer as output. The integer returned as output contains the current size of the bank being located. Therefore, should we wish to locate an arbitrary bank containing five data elements, then the value of *bank_size* would be five. This variable allows the programmer to iterate through the bank data without going over the boundaries of the bank in memory, which would cause a segmentation fault [20].

The returned size variable does not allow the programmer access to the actual data within the bank, only to the quantity of data stored. To retrieve and perform calculations on the data within a MIDAS bank the arguments depicted in the "*bk_locate*" method call above are necessary. The argument, *pevent*, is a pointer to the current event. This is necessary as the bank contents change every event. Therefore, should the event pointer variable point to some other undesired event, then all data read from the bank would not pertain to the current event, which is logically what the experimenter would want. The event pointer can be crudely thought of as timing information as the banks are filled every event and the events change over time, so that the contents of the banks must also change over time.

In addition to knowing for which event we would like the bank contents, we also need to know which bank we would like access to. This information is located in the second argument of the locate method. During the creation of each bank, the user must provide MIDAS with certain information. One of these pieces of information is a four character string used to identify the bank. This string is then passed as an argument to the locate method so that MIDAS can differentiate between all accessible banks. In the single-line code excerpt above the bank name is $TDC0$.

At this point MIDAS now has enough information to retrieve the desired bank data for the current event. However, there is as yet no means of passing that bank data back to the user. The third and final argument of the locate method provides a means of relaying the information retrieved from the bank back to the programmer. As passing a potentially large amount of information from one point in the MIDAS program to another could be very expensive computationally, MIDAS requires that the programmer provides a reference, capable of pointing to an arbitrary memory location, so that MIDAS itself can point the user-supplied reference to the area in memory where the desired data is stored, thereby allowing the user to iterate through that data by iterating the reference.

5.4.3 Correcting the Raw TDC Time Data for Differences in Processor Speeds

As was mentioned previously, the CAEN V1190 TDC modules are a new addition to the focal-plane detector package at iThemba LABS and were purchased, in part, because of the potential high resolution that these TDCs offer and also because the manufacturers of the old TDC modules, LeCroy, are no longer in business.

The high-performance microprocessors used in the CAEN V1190 TDC modules operate at 320MHz [18], while the processor used to drive the triggering hardware only operates at a frequency of 40MHz. This causes problems with data acquisition as the current TDC modules send time data faster than the system can register it. Consider a TDC event triggered at the very beginning of the main CPU's 40MHz clock cycle. The control system would not register that event until the end of the current system clock cycle, resulting in the event being offset by as much as 25ns ($T = 1/40\text{MHz}$). This 25ns jitter in the raw TDC data is shown in Figure 5.2.

To correct for this difference in operating frequencies both the control system and the TDC processors are kept in a phase locked loop (PLL). A phase locked loop is defined as a control system that generates a signal that has known and fixed relation to the phase of a reference signal [11]. A circuit in a phase locked loop responds to both the frequency and phase of an input signal and automatically raises or lowers the frequency of a controlled oscillator until it matches the reference signal in both frequency and phase [28].

Employing this phase locked loop allows the slow 40MHz system processor to achieve the same resolution as the fast 320MHz TDC modules. The result of the phase locked loop is that every TDC module stores timing offset information to a unique channel in the TDC module. This timing offset information gives the experimenter access to when in the 40MHz main system cycle the current event was triggered. This allows the experimenter to subtract the

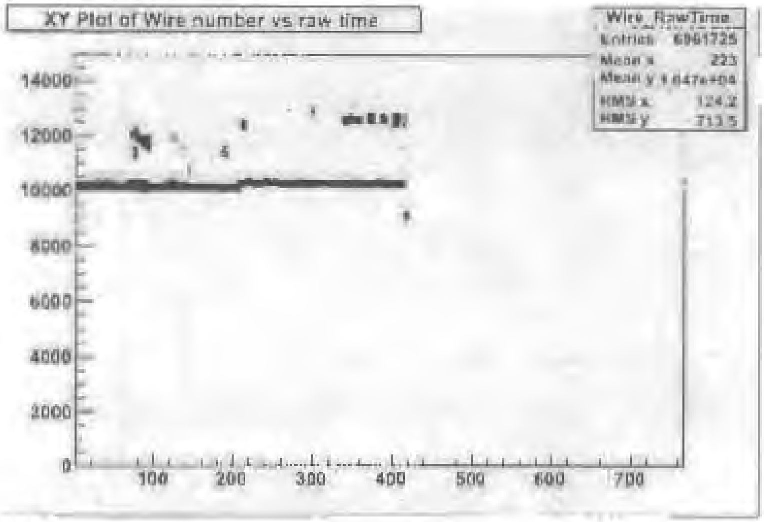

Figure 5.2: Raw wire number and time data for pulser run number 459.

offset from the event information to resolve when in the 40MHz cycle it occurred, thus eliminating the 25ns jitter seen in Figure 5.2. The corrected raw data spectrum is shown in Figure 5.3.

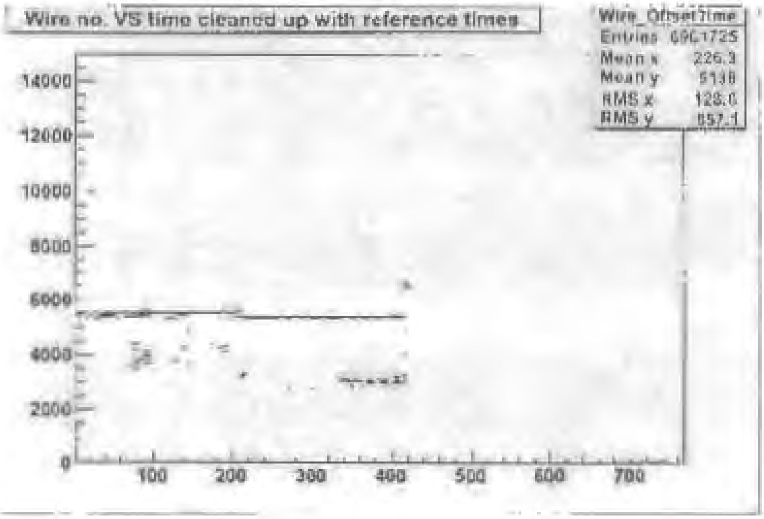

Figure 5.3: Raw wire number and time refined with TDC offset data for pulser run number 459.

As can be seen from Figure 5.3 the timing resolution of the raw data spectrum (seen here as vertical thickness) is significantly better than in Figure 5.2.

Table 5.2 illustrates the TDC module offset to channel map.

TDC module No.	Channel No.
1	600
2	601
3	602
4	603
5	604
6	605

Table 5.2: TDC module offset to channel map.

If one examines Figure 5.2, one notices a structure in the y-axis data. The structure that appears at around $1200\mu s$ on the y-axis is the result of corrupted raw wire data from faulty channels within the detector (to be explained in Chapter 6). To aid the experimenter to recognise corrupted raw wire data, the analyser module assigns all event data collected from unstable channels a large value relative to the rest of the collected data set. Information collected from these events is not used in the calculation of physical observables.

When subtracting the offset data from the event data one could perform the subtraction in such a way so as to have either a positive or a negative result. The convention in the developed analyser module was to perform the subtraction so as to have a positive result. Performing the subtraction in this order is responsible for the shift in the y-axis data observed when comparing Figure 5.2 to Figure 5.3. The general lowering and thinning out of the time data on the y-axis is the intended result of the offset data subtraction.

5.4.4 Correcting for Physical Cabling Effects

If we re-plot Figure 5.3 and set the range of the vertical axis from 5250 to 5600ns we observe that not all pulser signals were received by the data acquisition system at the same time. When the system is operated in test-pulse mode however, it stands to reason that all wires within their own wire-planes should fire at precisely the same time as they were sent the test pulse at precisely the same time.

The timing offsets resulting from cable effects can be observed in Figure 5.4. These offsets are large enough to adversely effect the results of a experiment and, in a complete analyser, ought to be corrected for.

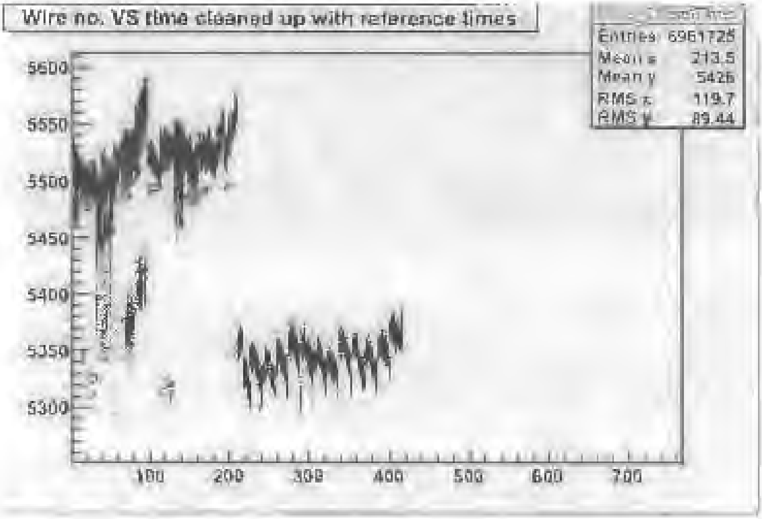

Figure 5.4: Raw wire number and time refined with TDC offset data for pulser run number 459 magnified to illustrate cabling effects.

The easiest way to correct for these cabling effects is to fit a Gaussian distribution to every wire that fired on a per drift-chamber basis in test pulse mode, store the means of these Gaussian distributions and calculate the mean of the means. Once the mean of the means has been calculated, the Gaussian peaks are all shifted until they are all of them equal to the mean of the means. The offsets resulting from these various shifts are then saved to an array and subtracted from the relevant channel when the system is operating in data-capture mode.

An example single wire spectrum is depicted in Figure 5.5.

The effect that this cable offset calculation has on the collected raw data can be seen in Figures 5.6 and 5.7.

5.4.5 Sorting Data into Correct TDC Data Structures

Now that the analyser is capable of accessing the data read as input from the electronics and packaged by the front-end system, the next logical step is to sort and collate that data into a form convenient for both data analysis and potential debugging or data dumping. The most common technique used to design a computer programme based on an existing physical system is to model the constituents of that existing system within the programme

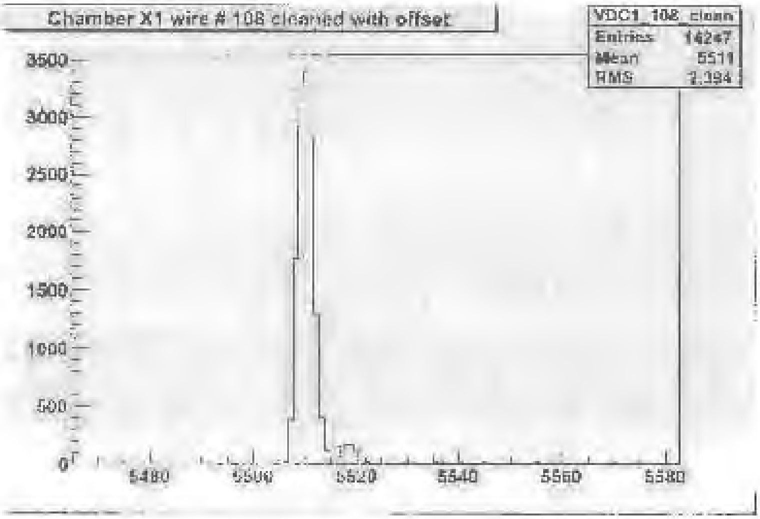

Figure 5.5: A sample single wire spectrum from test pulse run number 459.

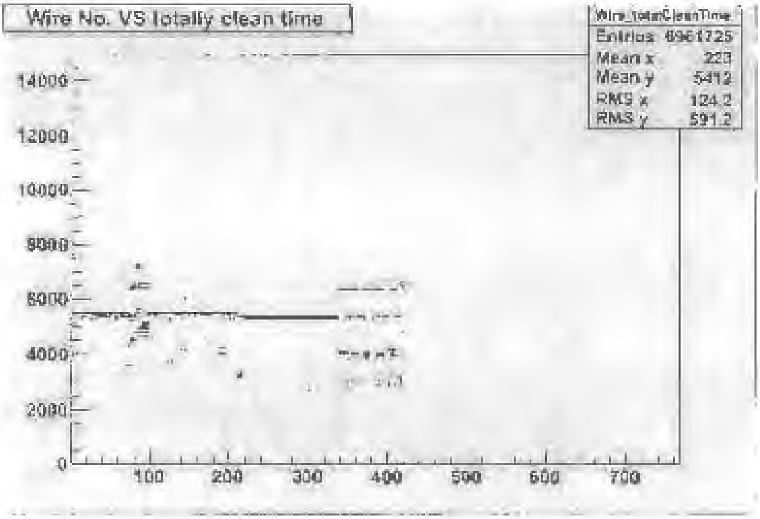

Figure 5.6: Cleaned up raw data spectrum with cable effects compensated for. The data is from pulser run 459.

code. Applying this technique to the analyser implies that the focal-plane package should, to a degree, be represented computationally. As there are two MWPCs, each containing two wire-planes, the decision was made to model the individual wire-planes and relate these to the MWPCs by naming the variables representing the wire-planes appropriately.

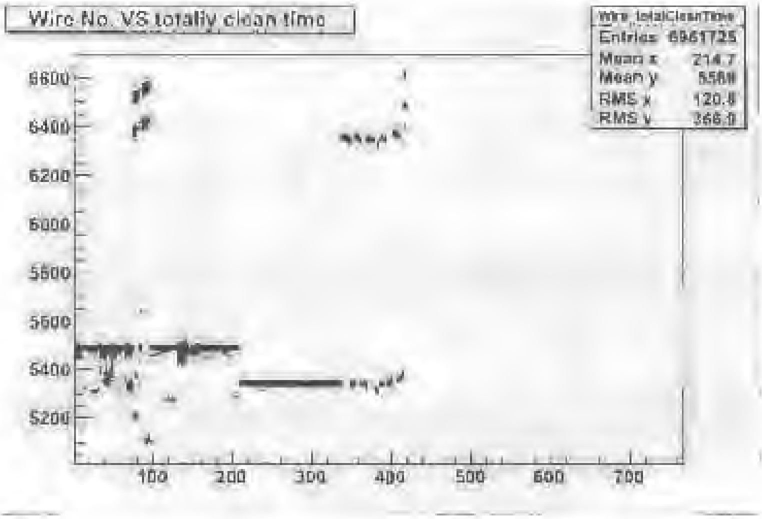

Figure 5.7: Cleaned up raw data spectrum with cable effects compensated for and vertical axis re-scaled. The data is from pulser run 459.

The data structure chosen to store the wire-plane and MWPC data was an array of integers. The reason for this is that the drift time, when measured in nanoseconds, is an integer number and so too is the number of the channel that fired. The integer arrays themselves are of a fixed size. The reason for this is that there exists a maximum number of wires that are allowed to fire in a single event before the event is deemed invalid [33]. This implies that the maximum length of any of the channel arrays must be equal to the maximum number of allowed wires per event. As the channel data and drift time data form a tuple, it follows that the maximum length of any of the drift time arrays must also be equal to the maximum number of allowed channels per event.

For the K600 magnetic spectrometer, the maximum number of allowed channels per event is eight [30]. Therefore the length of all drift chamber storage arrays is chosen to be eight, or, at least, chosen to be a variable which is defined to be eight at the beginning of the program, so that correct event data analysis is ensured for all event data. The arrays used to store all event data prior to analysis are as follows:

```
int VDC1_CHAN[MAX_WIRES_PER_EVENT]
int VDC1_TIME[MAX_WIRES_PER_EVENT]
```

These two integer arrays are used to store event data for the X-plane of the first MWPC. The first array stores the channel or wire-number data and the second array stores the drift times associated with the wire or channel data.

```
int VDC2_CHAN[MAX_WIRES_PER_EVENT]
int VDC2_TIME[MAX_WIRES_PER_EVENT]
```

These two integer arrays are used to store event data for the X-plane of the second MWPC. As before, the two arrays correspond to the wire-number and drift time data respectively.

```
int VDC3_CHAN[MAX_WIRES_PER_EVENT]
int VDC3_TIME[MAX_WIRES_PER_EVENT]
```

The above two integer arrays are used to store event and channel data for the U-plane of the first MWPC.

```
int VDC4_CHAN[MAX_WIRES_PER_EVENT]
int VDC4_TIME[MAX_WIRES_PER_EVENT]
```

The final two integer arrays shown above are used to store event and channel data for the U-plane of the second MWPC. The arrays depicted above still have to be filled, however, and this is done by way of the online database. As mentioned before, the TDC to wire-number map is read from the online database, allowing the analyser program to correctly identify which TDC channel corresponds to which wire in all four wire-planes. Once the TDC channel numbers have been resolved to wire-numbers, the analyser program can then fill the CHAN arrays depicted above as the wire-plane to wirenumber map is known.

5.4.6 Methods Used to Check TDC Data Correctness

At this point in the analyser program the channel and drift data arrays are filled correctly. There is, however, a chance that the correctly sorted event data could represent an invalid event. For this reason the channel arrays are checked against a list of predefined criteria to ensure that the event data is useable. This list of criteria is presented below [30]:

- At least three wires in any wire-plane must fire per event.

- No more than eight wires may fire in any wire-plane per event.
- There must not be a gap larger than one in between wires that fired.

Implementation of the first two criteria was accomplished by creating and updating the following four variables:

vdc1_hits, *vdc2_hits*, *vdc3_hits*, *vdc4_hits*.

As the names suggests, *vdc1_hits* stores the number of wires that fired in the X-plane of the first MWPC on a per-event basis, while *vdc2_hits* stores the same information for the X-plane of the second MWPC. The remaining two variables, *vdc3_hits* and *vdc4_hits*, store the number of wires that fired in the U-planes of MWPC one and two respectively on a per-event basis. These variables are incremented during the data sorting procedure explained above. Every time a *VDC_X_CHAN* array has a member added to it, the appropriate hits variable is incremented.

After all data has been sorted into the appropriate channel and data arrays, the values of the corresponding hits variables are checked against the first two elements in the above list via simple algebraic comparisons. As there is both a lower and an upper bound on the number of wires that must fire in all four wire-planes, there will be a total of eight comparisons all of which must be true. These comparisons look as follows:

```
if ((vdc1_hits > MAX_WIRES_PER_EVENT) ||
(vdc1_hits < MIN_WIRES_PER_EVENT)     ||
(vdc2_hits > MAX_WIRES_PER_EVENT)     ||
(vdc2_hits < MIN_WIRES_PER_EVENT))    ||
(vdc3_hits > MAX_WIRES_PER_EVENT)     ||
(vdc3_hits < MIN_WIRES_PER_EVENT))    ||
(vdc4_hits > MAX_WIRES_PER_EVENT)     ||
(vdc4_hits < MIN_WIRES_PER_EVENT))
clear_VDCS();
```

In addition to clearing the channel and data arrays when too many or too few wires have fired per event, the number of events rejected by these criteria is also recorded in separate variables for the sake of statistics and diagnostic purposes. These statistics are useful ones to keep track of as, if it is found that a large percentage of all incoming events is being rejected based on the number of wires that fired, then that would be a good indication to the experimenter to re-examine the experimental setup and machine calibration.

The variables responsible for storing these statistics are incremented as follows:

```
if ((vdc1_hits > MAX_WIRES_PER_EVENT) ||
(vdc1_hits < MIN_WIRES_PER_EVENT))
dc1_x_miss->Fill(vdc1_hits);
else if ((vdc2_hits > MAX_WIRES_PER_EVENT) ||
(vdc2_hits < MIN_WIRES_PER_EVENT))
dc2_x_miss->Fill(vdc2_hits);

if ((vdc3_hits > MAX_WIRES_PER_EVENT) ||
(vdc3_hits < MIN_WIRES_PER_EVENT))
dc1_u_miss->Fill(vdc3_hits);
else if ((vdc4_hits > MAX_WIRES_PER_EVENT) ||
(vdc4_hits < MIN_WIRES_PER_EVENT))
dc2_u_miss->Fill(vdc4_hits);
```

The values of the *miss* variables are then added to histograms so that they can be more easily interpreted by the experimenter.

After this has been done the analyser then checks all wire-plane data to ensure that there is no gap larger than one between the wires that fired within each wire-plane. Any such gap would seem to suggest that more than one particle was incident on the MWPC in a single event, a scenario that is undesired and is therefore discarded. As before, should there be a gap larger than on in any wire-planee, all event data is cleared by the *clear_vdcs* method. The algorithm responsible for checking the gap between the wires that fired is as follows:

```
int c = VDC1_CHAN[0];
for (i=0; i<N; i++)
{
if (VDC1_CHAN[i] - c <= 2) c = VDC1_CHAN[i];
else return 0;
}
```

The code excerpt shown above is used to calculate the gap in the X-plane of the first MWPC and is taken from the *check_tdcs* method located in the analyser. All pairs of wire-numbers in the channel array are compared to each other by value and, should a gap of more than one be detected, the method will return zero. When the analyser receives a zero from the *check_tdcs* method, it then calls the *clear_VDCS* method described above.

Similar code fragments perform the same calculations on the three remaining wire-planes in a single pass. Therefore, should any wire-plane possess a gap of more than one wire in the list of wires that fired for a single event, the *clear_VDCS* method would return zero immediately, negating the need for further calculations on the remaining wire-planes.

5.4.7 Implementing the Line-fitting Techniques

At this point in the analyser's execution all event data has been checked for correctness and packaged into the appropriate data structures. The event data structures and their units are shown in Table 5.3.

Data Structure Name	Unit
vdc1_chan (Channel data for X1)	Wire number
vdc1_time (Drift time data for X1)	μs
vdc2_chan (Channel data for X2)	Wire number
vdc2_time (Drift time data for X2)	μs
vdc3_chan (Channel data for U1)	Wire number
vdc3_time (Drift time data for U1)	μs
vdc4_chan (Channel data for U2)	Wire number
vdc4_time (Drift time data for U2)	μs

Table 5.3: Analyser event data structures and their units.

In order to accurately apply the line-fitting techniques explained in Chapter 3, we need both variables to be of the same type. Table 5.3 shows that the channel array is in units of wire number, which is analogous to distance, while the data or time array is in units of μs. In order to reconstruct the particle's trajectory, both arrays must be in units of distance.

As stated previously, the drift time in the MWPCs is proportional to drift distance and can be converted into drift distance by means of a look up table. The look up table takes a drift time as input and returns the corresponding drift distance as output. This look up table is necessary as the MWPCs at iThemba LABS are not conventional in the sense that the drift velocity is not constant, but rather possesses a $1/r$ dependence when close to an anode wire [33]. The role of the look up table is therefore to compensate for this changing drift velocity and allow the experimenter access to the correct drift distances. The look up table used with the MWPCs at iThemba LABS is shown in Figure 5.8.

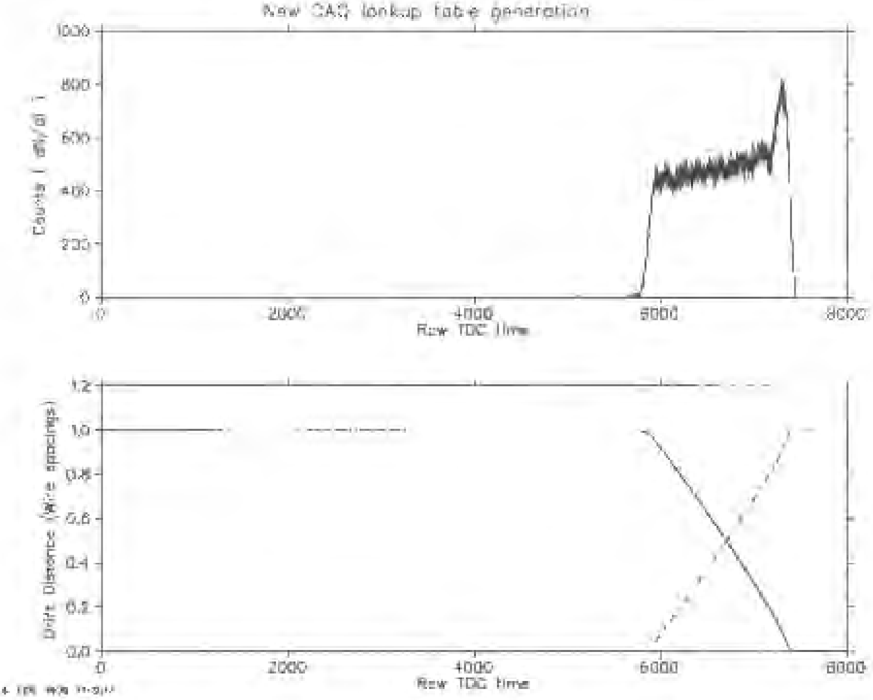

Figure 5.8: A visualisation of the look up table used in the new data acquisition system. The image above shows the experimental data used to generate the look up table, while the image below shows the completed look up table [32].

The visualisation depicted in Figure 5.8 is a graphical representation of the data file used to convert drift times to drift distances. The file used by the analyser comprises one column of data, whose length spans the entire x-axis and whose values span the y-axis of the second part of Figure 5.8.

During the initialisation phase of the analyser program, this data file is loaded into an array whose length is equal to the number of rows in the file. What results is an array with the number of entries exactly equal to the allowable drift times, while the entries themselves are the distances that ionised electrons would have drifted during those drift times.

As an example, consider a single-wire event where the drift time measured was 6000ns. To compute the drift distance associated with a drift time of

6000ns, one would set the drift distance equal to the 6000^{th} entry in the look up table. Should the drift time have been 8000ns, one would set the drift distance equal to the 8000^{th} entry in the look up table.

Once the drift times have been resolved to their respective drift distances, the line-fitting algorithms outlined in Chapter 3 can be applied and the desired spectral data added to histogram data structures and displayed to the experimenter.

Chapter 6

Testing the Analyser

Now that the analyser raw data has been corrected for various hardware and physical constraints, all that remains to be seen is whether or not the techniques outlined in Chapters 3 and 4 have resulted in a working analyser module. The most intuitive method of checking the customised analyser module for correctness is to compare it to known spectra from another system.

Unfortunately, at the time of writing, the new detectors were not functioning with the new MIDAS software. The current system at iThemba LABS functions either with the new detector electronics but the old data acquisition software or with the new data acquisition software with the old detector electronics. For the purposes of this project however, testing the effectiveness of the new analyser module with the old detectors was deemed more relevant as the vertical wire, or X, plane of the old detectors is the same as the X-plane of the new detectors.

Unfortunately this implies that the methods used to reconstruct the trajectory of the incident particles perpendicular to the focal-plane cannot be carried out. There is some consolation, however, as the line-fitting techniques used to reconstruct the position of the incident particles in the plane of the focal-plane are the same as those used in the plane perpendicular to the focal-plane. Therefore, proving that the focal-plane information calculated by the analyser is correct in itself implies that the methods used to calculate information perpendicular to the focal-plane are also likely to work, when the experimental data becomes available to test this.

The first step in checking the analyser module for correctness is to ensure that the raw data gathered by the analyser is in fact correct. To check this the raw data spectrum calculated from run number 436 is compared to the raw data spectrum for the same experiment generated at iThemba LABS. These two graphs should not only be similar, but rather identical. The two raw data spectra are shown in Figures 6.1 and 6.2.

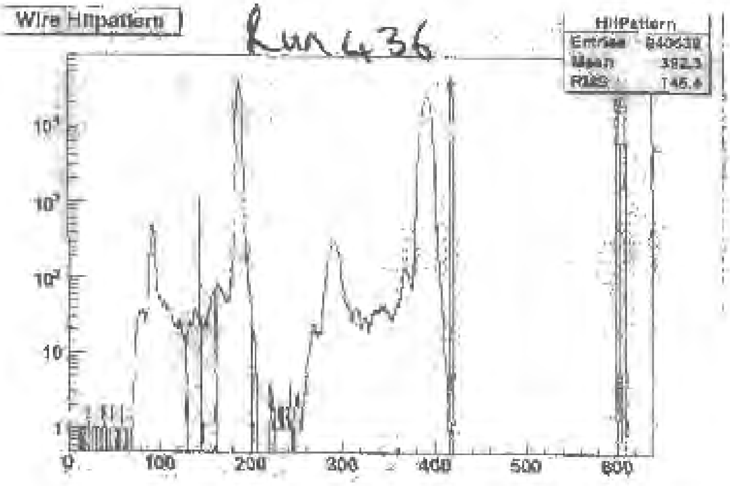

Figure 6.1: A plot of the wire hit pattern for run number 436 taken from the iThemba LABS data book with the y-axis in logarithmic scale.

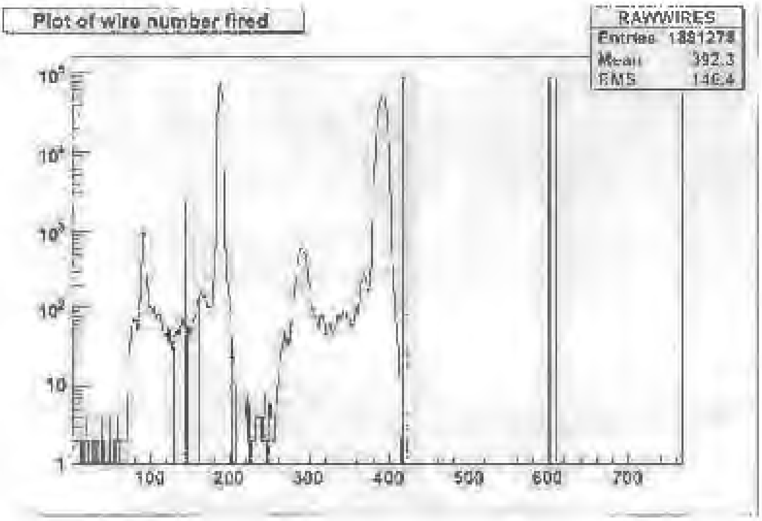

Figure 6.2: A plot of the wire hit pattern calculated by the new MIDAS analyser for run number 436 with the y-axis in logarithmic scale.

Figures 6.1 and 6.2 agree exactly, as is required. To ensure that this is not merely a coincidence the wire hit patterns from the new MIDAS analyser and iThemba LABS are compared again with data from experimental run number 437. Figures 6.3 and 6.4 depict the comparison.

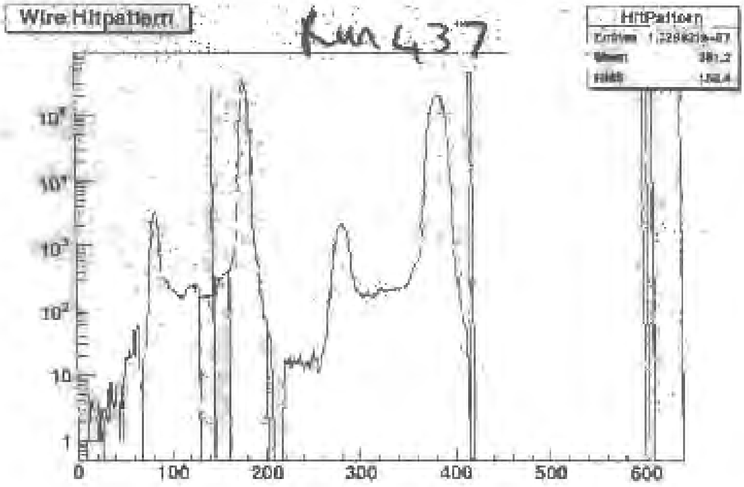

Figure 6.3: A plot of the wire hit pattern for run number 437 taken from the iThemba LABS data book with the y-axis in logarithmic scale.

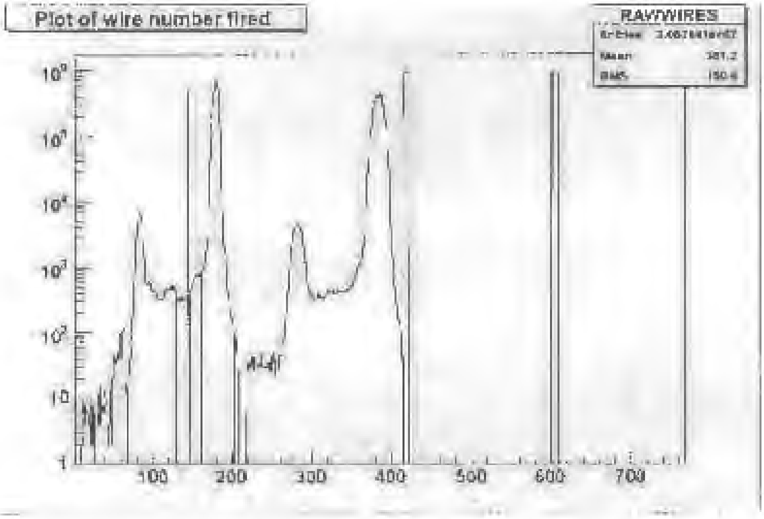

Figure 6.4: A plot of the wire hit pattern calculated by the new MIDAS analyser for run number 437 with the y-axis in logarithmic scale.

Once again we observe that the spectra match each other perfectly. This implies that the portion of the new analyser module responsible for collection and processing of the raw data works correctly. The only test remaining is whether or not the calculated position spectra match the raw data, which is now known to be correct.

The calculated position spectrum in the plane of the focal-plane from run number 437 is presented in Figure 6.5.

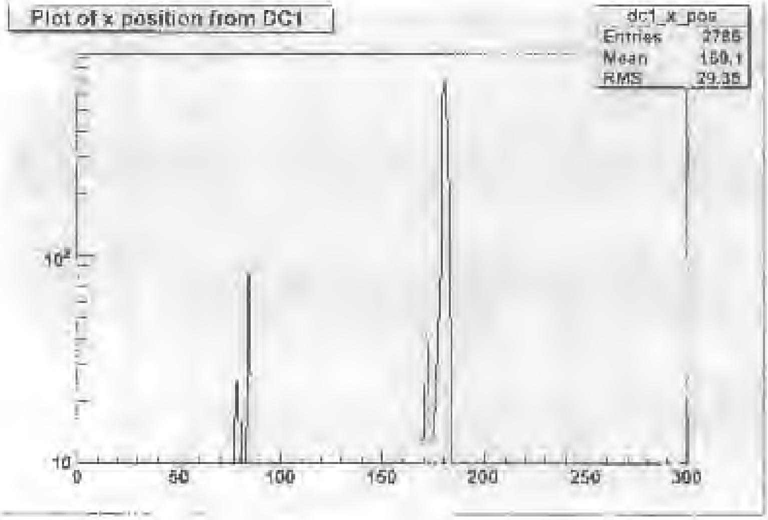

Figure 6.5: A plot of focal-plane position calculated from the first horizontal wire-plane from run 437 with the y-axis in logarithmic scale.

Experimental run number 437 consisted of a proton beam, with a beam current of 1nA, incident on a ^{12}C target with a thickness of approximately 40 – 45 mg.cm^{-2}. The carbon target however was not pure and contained ^{13}C impurities of the order of 1 part in 1000.

Figure 6.5 displays the mean position spectrum calculated from the X-plane of the first detector. The second X-plane and the vertical plane were not considered as they were known to yield flawed data [33, 32]. This is confirmed by the breadth of the peaks in the second drift chamber and the complete lack of usable data in the HDC. The spikes observed between channels 600 and 605 are the offset data described in §5.4.3 and the spike observed at wire 145 is the result of a noisy channel [33].

The remaining peaks, corresponding to the physical experimental information, occur at wire numbers 85, 120, 172, 178. The position peaks, as calculated by the analyser code, were found to be at wire numbers 85, 172, 178. The first peak in the position spectrum, located before the peaks at wire numbers 85–178, is considered to be part of the background as it is relatively small, even when viewed on a logarithmic scale.

The second peak in the position spectrum, located at wire number 85 corresponds to the first excited state of ^{12}C [32, 34]. The third peak seen in the raw data spectrum, located at wire number 120, is not seen in the position spectrum. The reason for this is two-fold: Firstly, channel number 130 was not operational during this run and secondly, the calibration data generated from run number 459 was flawed in this region. These two factors forced the data analysis software to disregard these events and treat them as though they were invalid. Figure 6.6 illustrates an example wire that resulted in bad calibration data.

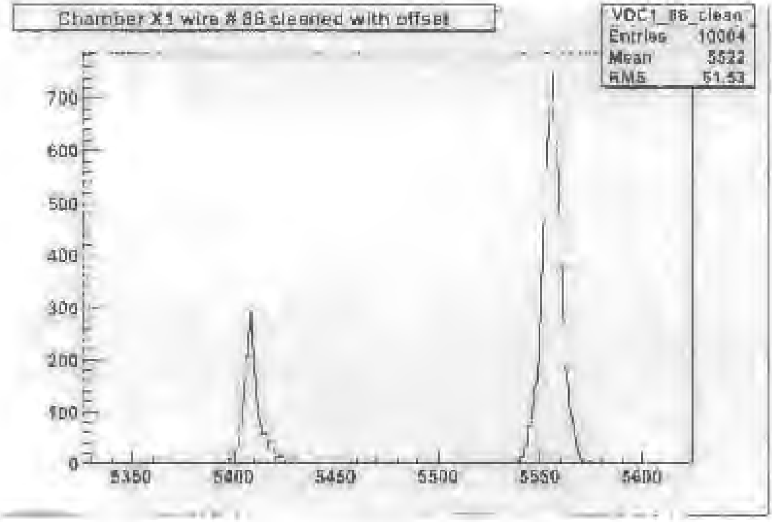

Figure 6.6: A plot of the single wire spectrum for wire 123 from test pulse run number 459. The smaller of the two peaks, centred at 5410, should not have resulted from a pulser run and is consequently ignored by the analyser. This unfortunately renders the wire unusable by the analyser module.

The next peak observable in the position spectrum is located at wire number 172. In the raw data spectrum wire number 172 is the shoulder to the peak observable at wire number 178 and corresponds to the ground state energy of the ^{13}C impurities in the ^{12}C target [32, 34].

The final, and largest peak, found at wire number 178 in the raw data spectrum corresponds to the ground state of ^{12}C [32, 34].

Checking the calculated focal-plane angular information, however, is not as simple. A standard approach would consist of calculating the focal-plane angles from both the first and second drift chambers and comparing these to each other, to check for continuity. In the absence of data from the second drift chamber, the most reliable means of ascertaining focal-plane angle correctness is to examine the full width of the Gaussian at half of its maximum value [32].

This value is known to be between 7 and 8 degrees [32, 34]. Figure 6.7 illustrates the calculated focal-plane angle spectrum, calculated from the first drift chamber, from run number 437. The angular distribution, calculated as the full width of the Gaussian at half of the maximum value, was found to be 7.472°, which falls within the interval supplied by iThemba LABS.

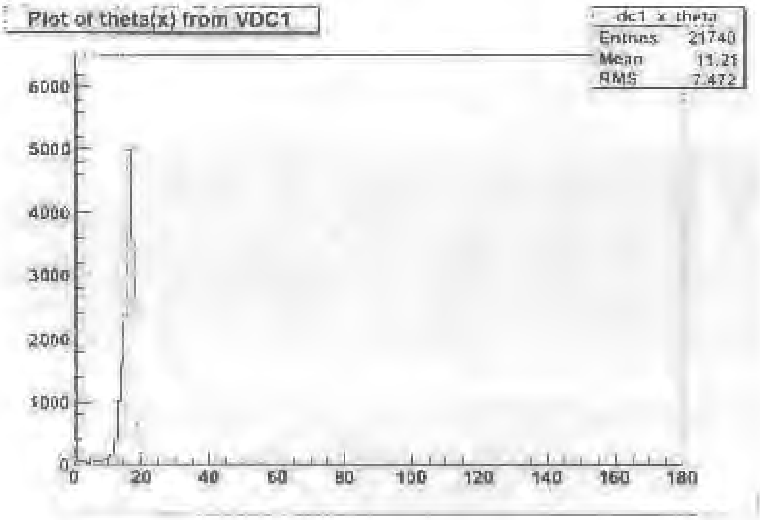

Figure 6.7: A plot of calculated focal-plane angles in the first drift chamber, taken from run number 437. The x-axis here is in units of degrees.

Having demonstrated that the customised analyser developed in this thesis reproduces raw data spectra exactly when compared to those generated at iThemba LABS and that the position and angle information, calculated by the line-fitting techniques and trajectory reconstruction algorithms, agrees with experiment, the customised analyser module is deemed to work satisfactorily.

Chapter 7

Conclusions and Further Developments

In this thesis, the underlying principles behind proportional counters and multi-wire proportional counters were thoroughly reviewed, both in theory and design. These ideas were then extended to both standard horizontal and vertical drift chambers, and the non-standard drift chambers currently in operation at iThemba LABS. Mention was made of the changes recently made to the focal-plane detector package at iThemba LABS. The mathematical methods used to generate physical data such as position, both in the focal-plane as well as perpendicular to the focal-plane, were presented.

A new analyser module, intended to operate within the recently upgraded detector package was proposed, and both the conceptual and software designs of this analyser were outlined in detail. Included was a concise description of the software environment in which the analyser was designed to operate (MIDAS), as well as the additions to the software framework necessary to facilitate the integration of the new module into the existing ones. The internal functionality of the analyser was explained, together with the methods used for calibration and cabling effects.

Finally, the new analyser module was tested against both pulser and experimental data, and was found to be working satisfactorily. The raw data spectra produced by the analyser were compared to those taken from the K600 experiment logbook and found to agree. In addition, the position and angle spectra calculated by the new analyser module were themselves examined and determined to be consistent with experiment.

The working analyser module will be integrated into the new data acquisition system at iThemba LABS[1] and will be responsible for the calculation of basic focal-plane information common to all experiments carried out on the K600 magnetic spectrometer. As mentioned previously, the newly upgraded detector package is not yet completely operational. The current schedule places the first data capturing run of the new detectors in June 2008 [33, 32], which will allow the analyser module developed in this thesis to be implemented.

Further developments to the analyser module include a wider range of histograms available to the experimenter, as well as complete testing of the algorithm used to extract vertical information from the slanted wire-planes. Currently this cannot be tested as, at the time of submission, no data was available for the new detector package.

---

[1] A complete copy of the source code is available at iThemba LABS, Cape Town.

Bibliography

[1] W.R. Leo, "Techniques for Nuclear and Particle Physics Experiments", Springer-Verlag, 1987.

[2] B. Jean-Marie, V. Lepeltier and D. L'Hote, "Nuclear Instrumentation and Methods", **159**, 213, 1979.

[3] A.C. Melissinos, "Experiments in modern Physics", Academic Press, New York, 1966.

[4] M.F. L'Annunziata, "Handbook of Radioactivity Analysis", Academic Press, New York, 2003.

[5] P.R. Bevington, "Data Reduction and Error Analysis for the Physical Sciences", New York: McGraw-Hill, 1969.

[6] "Numerical Recipes: The Art of Scientific Computing", Cambridge University Press, 2007.

[7] R. Garsideand and J. Mariani, "Java: first contact", Course Technology, 1998.

[8] L. Underhill and D. Bradford, "IntroSTAT", Juta, 2000.

[9] B.R. Martin,"Statistics for physicists", London: Academic Press, 1971

[10] H. Abelson, G.J. Sussman and J. Sussman, "Structure and Interpretation of Computer Programs", MIT Press, 1996.

[11] R. E. Best, "Phase-locked Loops: Design, Simulation and Applications", McGraw-Hill, 2003.

[12] A. Shevchenko, "Fine Structure of the Isoscalar Giant Quadrupole Resonance from High-Resolution Inelastic Proton Scattering Experiments", PhD thesis, University of Darmstadt, 2005.

[13] R. Neveling, "The Drift Chamber U-plane", Unpublished, 2005.

[14] R. Alfaro, "Construction and operation of a small multi-wire proportional chamber", Journal of Physics: Conference Proceedings **18**, 362, 2005.

[15] F. Sauli, "Principles of Operation of Multi-wire Proportional and Drift Chambers", Lectures given in the Academic Training Programme, CERN, 1977.

[16] Bertozzi et al, "Nuclear Instrumentation and Methods", **141**, 141, 1977.

[17] D. Glaser, "Some Effects of Ionizing Radiation on the Formation of Bubbles in Liquids", Phys. Rev. 87 (4): 665 - 665, 1952.

[18] "V1190 TDC Technical Information Manual", Revision n.5, CERN, 2004.

[19] "A DRAFT Guide to the K600 Magnetic Spectrometer", Unpublished, 2006.

[20] "Maximum Integrated Data Acquisition System (MIDAS) Manual", `https://midas.psi.ch/htmldoc/index.html`.

[21] Hamamatsu, R329-02 Photomultiplier Tube datasheet, 314-5, Shimokanzo, Toyooka-village, Iwata-gun, Shizuoka-ken, 438-0193, Japan, 1999.

[22] S. Fine et al., "Proportional Counter", United States Patent Office, Patent number 3092747, 1963.

[23] L.G. Christophorou et al., "Gas mixtures for gas-filled particle detectors", United States Patent Office, Patent number 4201692, 1980.

[24] iThemba LABS webpage: `http://www.tlabs.ac.za/public/default.htm`

[25] Nobel press release, "The Nobel Prize in Physics 1992", `http://nobelprize.org/nobel_prizes/physics/laureates/1992/press.html`.

[26] Iowa State University, Centre for Nondestructive Evaluation, `www.ndt-ed.org/educationresources/communitycollege/radiography/physics/ionization.htm`

[27] Quark Net, `http://quarknet.fnal.gov/projects/pmt/student/tenstage.shtml`.

[28] Wikipedia, `http://en.wikipedia.org/wiki/Phase-locked_loop`.

[29] Stephen Wolfram's Mathworld, `http://mathworld.wolfram.com/LeastSquaresFitting.html`.

[30] R.W. Fearick, Private communication.

[31] F.D. Smit, Private communication.

[32] R. Neveling, Private communication.

[33] S. Murray, Private communication.

[34] H. Fujita, Private communication.

Acknowledgments

I would like to thank my supervisor, Prof. Roger Fearick, for his encouragement and assistance throughout all stages of this thesis.

I would also like to thank the K600 research group, in particular Dr R. Neveling, Dr. F.D. Smit and Dr H. Fujita for their knowledge and support.

To Sean Murray, for assisting me with MIDAS issues and for your limitless patience I thank you.

I am grateful to Andrea Prinsloo and Maciek Stankiewicz for their invaluable editing contributions at the final stages of this thesis.

I would like to thank the Board of Executors for their financial assistance.

To my family and Raegan Murphy: You have provided me with love and support but most of all you have tolerated my odd behaviour and strange hours throughout the past three years and, from the bottom of my heart, I thank you.